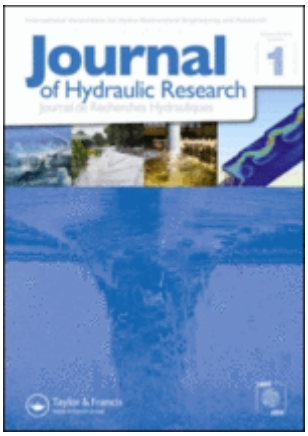

Flow and turbulence of free-surface flow over a backward-facing step

Journal:	*Journal of Hydraulic Research*
Manuscript ID	TJHR-2021-0170.R3
Manuscript Type:	Research paper
Date Submitted by the Author:	12-Jul-2023
Complete List of Authors:	Luo, Qianyu; University College London Department of Civil Environmental and Geomatic Engineering, Department of Civil Environmental and Geomatic Engineering Stoesser, Thorsten; University College London Department of Civil Environmental and Geomatic Engineering, Department of Civil Environmental and Geomatic Engineering ; Georgia Institute of Technology Jalalabadi, Rzieh; University College London Department of Civil Environmental and Geomatic Engineering, Department of Civil Environmental and Geomatic Engineering Xie, Zhihua; Cardiff University, School of Engineering
Keywords:	Backward Facing Step, Free surface flow, Kinetic Energy Balance, Large eddy simulation, Separation
JHR Keywords:	Large Eddy Simulations < Turbulent flows, Open channel flow turbulence < Turbulent flows, Separated flows < Vortex dynamics; rotating fluids
Note: The following files were submitted by the author for peer review, but cannot be converted to PDF. You must view these files (e.g. movies) online.	
APA-JHR.bib tJHRguide.tex	

To appear in the *Journal of Hydraulic Research*
Vol. 00, No. 00, Month 20XX, 1–19

Research paper

Hydrodynamics and turbulence of free-surface flow over a backward-facing step

QIANYU LUO (IAHR Member), Research Associate, *Department of Civil, Environmental and Geomatic Engineering, University College London, London, UK*
Email: qianyu.luo.18@ucl.ac.uk

THORSTEN STOESSER (IAHR Member), Professor, *Department of Civil, Environmental and Geomatic Engineering, University College London, London, UK*
Email: t.stoesser@ucl.ac.uk (author for correspondence)

RAZIEH JALALABADI, Research Associate, *Department of Civil, Environmental and Geomatic Engineering, University College London, London, UK*
Email: r.jalalabadi@ucl.ac.uk

ZHIHUA XIE (IAHR Member), Reader, *School of Engineering, Cardiff University, The Parade, Cardiff CF24 3AA, UK*
Email: z.xie@cardiff.ac.uk

Running Head (Free-surface flows over a backward-facing step)

Hydrodynamics and turbulence of free-surface flow over a backward-facing step

ABSTRACT
Three large-eddy simulations of open channel flow over a backward-facing step are performed to investigate the effect of submergence on the turbulence, hydrodynamics, and water surface deformation downstream of the step. The deformation of the water surface, the extent of the recirculation zone as well as the strength of the shear layer are a function of relative submergence. All flows downstream of the step exhibit elevated levels of turbulent shear stress and contain significant amounts of turbulent kinetic energy. The instantaneous flow features rollers immediately behind the step and horseshoe-shaped vortices shed from the shear layer, the latter being advected towards the water surface where they cause deformations. It is shown that these vortices can originate from any location along the dividing streamline, however, they contain more energy the closer to the mean attachment location they originate.

Keywords: Backward-facing step; free surface; large-eddy simulation; relative submergence; turbulence

1 Introduction

The flow over a backward-facing step is a well-known representative of flow separation and reattachment hydrodynamics. A large number of studies have been carried out on this flow due to its geometrical simplicity yet complex hydrodynamics featuring flow separation, recirculation, adverse pressure gradient, flow reattachment and boundary layer recovery. Similar flows to a backward-facing step flow are ubiquitous in nature such as the flow over sand dunes or over natural beds with large-scale geomorphological features (e.g. step-pool systems) or over hydraulic structures such as broad-crested weir flows (Nakagawa and Nezu, 1987). Besides, the step-generated turbulence in the flow brings strong spatial and temporal variability to the bed shear stress as well as elevated

Received 00 Month 20XX; accepted 00 Month 20XX/Currently open for discussion.

pressure fluctuations near the bed, which affects transport processes such as sediments, dissolved oxygen, pathogenic microorganisms etc. Therefore, flows through a sudden geometric expansion remain of fundamental research interest in hydraulics. Over the past decades, many experimental studies of the flow over a backward-facing step have been carried out. For instance, Jovic and Driver (1994) carried out an experiment in a wind tunnel with a double-sided symmetrical sudden expansion, confirming that backward-facing step (BFS) flows are sensitive to step height Reynolds number. In contrast to the aerodynamics community, BFS flows have received less attention in the hydraulics community and only few studies of free-surface BFS flows exist. Nakagawa and Nezu (1987) conducted a series of experiments of BFS open-channel flows for several expansion ratios E_r (defined as downstream-depth-to-upstream-depth-ratio), Reynolds numbers as well as Froude numbers. They employed a highly-accurate laser-Doppler anemometer to measure the velocity and provided extensive data sets including profiles of first- and second-order statistics at various locations. Clearly, the study of Nakagawa and Nezu (1987) is quite unique as it is one of the very few studies that investigated the flows over a backward-facing step in open channel flow where the water surface is the upper boundary. Ötügen (1991) investigated the effect of expansion ratio on flow reattachment while keeping upstream velocity, turbulence intensity as well as boundary layer thickness constant, showing that a larger expansion (i.e. lower submergence, where the submergence S is defined as downstream-depth-to-step-height-ratio) leads to more pronounced turbulent diffusion and consequently shorter reattachment.

Experimental studies have provided precious and comprehensive data sets which have been used to validate numerical methods and models. For instance, Le et al. (1997) performed calculations of turbulent flow over a backward-facing step in a duct via the method of direct numerical simulation (DNS), and achieved an excellent agreement with the experimental data of Jovic and Driver (1994). This DNS has served as a benchmark test case to the computational fluid dynamics community and is one of the most cited DNS to date. Friedrich and Arnal (1990) investigated the same flow but at a higher Reynolds number using large-eddy simulation, confirming the ability of LES to reproduce the behaviour of the instantaneous flow in the shear layer and the reattachment zone. Aider et al. (2007) examined the effects of upstream conditions using LES, demonstrating the necessity of imposing realistic time-dependent inlet conditions particularly in large-eddy simulations. Hu et al. (2016) employed their Improved Delayed Detached Eddy Simulation (IDES) technique and reported on the reattachment of the separated backward-facing step flow as being three-dimensional and highly unsteady.

Aforementioned research endeavours have been conducted to examine different aspects of backward-facing step flows. In general, the flow downstream of the step is characterised by the expansion ratio E_r, step height Reynolds number R_{eh}, or the state of the upstream boundary layer and its thickness (Adams and Johnston, 1988), respectively. Many studies investigated the effects of E_r, R_{eh}, or the upstream boundary layer characteristics on the reattachment length X_R. The wind tunnel study of Adams and Johnston (1988) at $E_r = 1.25$ and $\mathsf{R}_{\mathsf{eh}}= 8,000$ (and higher) demonstrated that the upstream-boundary-layer-thickness-to-step-height-ratio δ/h barely affects X_R/h as long as the upstream boundary layer is turbulent. The experiments of Nadge and Govardhan (2014) showed that X_R/h is constant for $\mathsf{R}_{\mathsf{eh}}> 36,000$ or when $Er > 1.84$ as long as upstream boundary layer is turbulent.

Similar to the backward-facing step where a sudden expansion occurs in the vertical (i.e. wall-normal) direction, the flow over lateral expansions (i.e. in spanwise) have also received significant attention (Babarutsi et al., 1989; Han et al., 2017, 2020). Although the recirculation due to the sudden expansion occurs in a different plane than their BFS counterpart their flows share similar characteristics. BFS flows are generally confined in the vertical whilst the spanwise confinement is negligible because of channel-width-to-step-height-ratio is usually greater than 10 (De Brederode, 1972). Lateral sudden expansions occur primarily in open channel flows for which the vertical confinement cannot be neglected. The bed friction-generated vertical shear plays a prominent role in the flow through sudden expansions (Han et al., 2020). In deep flows the bed friction has minor

impact on the recirculation zone behind a lateral sudden expansion, and hence such flows are comparable with BFS flows.

From the discussion above, it appears that the relative submergence S (or expansion ratio E_r) plays a significant role in the dynamics of flow separation and reattachment as well as boundary layer recovery. Moreover, only few studies to date have revealed details of the flow field in terms of first- and higher-order turbulence statistics at varying relative submergences while keeping the other key factors unchanged. Besides, the vast majority of the numerical studies to date deployed a rigid lid (i.e. free-slip condition) at a fixed water depth from upstream to downstream to approximate free-surface open channel flow over a backward-facing step, yet as Nakagawa and Nezu (1987) demonstrated there are time-averaged water surface deformations due to the sudden change in bathymetry as well as instantaneous water surface deformations due to the distinct step-generated large-scale turbulence. This paper reports on large-eddy simulations of open-channel free surface flow over a backward-facing step at various expansion ratios. The goal of this study is to quantify in high spatial resolution the effect of relative submergence on the hydrodynamics and turbulence in the expansion section of the channel, as well as to elucidate the interplay between the step-generated coherent structures and the surface deformations.

2 Numerical Framework

The open-source large-eddy simulation code Hydro3D is employed to perform the simulations. The code has been validated successfully for and applied to a number of similar problems, such as open-channel flows over rough beds (Liu et al., 2017; Nikora et al., 2019; Stoesser et al., 2015) and flow in a compound channel (Chua et al., 2019) or in partially-filled pipes (Liu et al., 2022a,b). The code solves the spatially filtered Navier-Stokes equations in an Eulerian framework reading:

$$\nabla \cdot \boldsymbol{u} = 0 \tag{1}$$

$$\frac{\partial \boldsymbol{u}}{\partial t} = -\frac{1}{\rho}\nabla p - \boldsymbol{u} \cdot \nabla \boldsymbol{u} + \nu \nabla^2 \boldsymbol{u} - \nabla \tau_{SGS} + \boldsymbol{f} + \boldsymbol{g} \tag{2}$$

where $\boldsymbol{u}$ denotes the filtered resolved velocity field, p denotes the pressure, ν is the kinematic viscosity, $\boldsymbol{f}$ represents the volume force exerted to the fluid by an external source and $\boldsymbol{g}$ is the gravitational acceleration. The sub-grid scale stress tensor, τ_{SGS}, results from unresolved small scale fluctuations, is approximated by the wall-adapting local eddy-viscosity (WALE) model (Nicoud and Ducros, 1999) for all the cases presented in this paper. Hydro3D is based on finite differences with staggered storage of three-dimensional velocity components and central storage of pressure on Cartesian grids.

The governing equations (1) and (2) are advanced in time by the fractional-step method (Chorin, 1968). In the predictor step, convection and diffusion terms are solved via an explicit three-step Runge–Kutta predictor. Fourth- and second-order central differences schemes are used to approximate convective and diffusive terms, respectively. In the corrector step the pressure and a divergence-free velocity field are obtained by solving the Poisson equation via a multigrid iteration scheme (Cevheri et al., 2016).

The water surface is captured by the level set method (LSM) proposed by Osher and Sethian (1988). The LSM introduces a level set signed distance function ϕ:

$$\phi(\mathbf{x}, t) < 0 \quad if \quad \mathbf{x} \in \Omega_{\text{gas}} \tag{3a}$$

$$\phi(\mathbf{x},t) = 0 \quad if \quad \mathbf{x} \in \Gamma \tag{3b}$$

$$\phi(\mathbf{x},t) > 0 \quad if \quad \mathbf{x} \in \Omega_{\text{liquid}} \tag{3c}$$

where Ω_{gas} and Ω_{liquid} represent air or fluid phases, respectively and Γ denotes the interface. The movement of the interface is expressed in a pure advection equation of the form:

$$\frac{\partial \phi}{\partial t} + \boldsymbol{u} \cdot \nabla \phi = 0 \tag{4}$$

A multi-phase transition zone is accomplished via a Heaviside function to handle the numerical instabilities brought by the density and viscosity discontinuities across the interface. In addition, the re-initialization technique proposed by Sussman et al. (1994) is employed to maintain $|\nabla \phi| = 1$ as time proceeds. A fifth-order weighted essentially non-oscillatory (WENO) scheme is chosen to discretise the equation (4) to ensure stability and minimize numerical dissipation for this pure advection equation. The validity of the LSM in the current code has been shown previously for various applications including open-channel flow over a cube and square bars (McSherry et al., 2017, 2018), and for flows past bridge abutments (Kara et al., 2015a,b).

Spatial-decomposition-based standard message passing interface (MPI) is used to accomplish the communications between pre-allocated computational subdomains. Such a technique is necessary to manage and balance the computational load to provide sufficiently fine grids in LES (Ouro et al., 2019).

3 Computational Setups and Boundary Conditions

3.1 *Validation experiments*

The large-eddy simulation method is validated first using laboratory experiments undertaken by Nakagawa and Nezu (1987). The experiment of Nakagawa and Nezu (1987) is considered for both validation of the turbulence statistics and the water surface elevation and is the basis for exploration of the effect of relative submergence S (downstream-depth-to-step-height-ratio, h_2/h) on the free-surface flow over a backward-facing step. In their experiment, an $h = 2cm$ high backward-facing step was placed $6.8m$ downstream of an $8m$ long, $30cm$ wide rectangular channel followed by a sufficiently long outlet channel up to $60h$ downstream of the step, which is considered to be long enough for the wake recovery behind the step. Two of the experiments are selected, which are ST1 and ST3, the flow conditions of which are provided in table 1. The step height Reynolds number $\mathsf{R_{eh}}$ is based on step height h and upstream spatially-averaged mean velocity U_{m1} (i.e., $\mathsf{R_{eh}} = U_{m1}h/\nu$), whereas the Froude number $\mathsf{F_r}$ is based on water depth downstream of the step h_2 and downstream spatially-averaged mean velocity U_{m2} (i.e., $\mathsf{F_r} = U_{m2}/\sqrt{gh_2}$). In these experiments the water surface elevation was measured with a point gauge which offered $1/20mm$-precision and velocity profiles were measured using an LDA system at selected locations along the centre line of the open-channel flume.

3.2 *Large-eddy simulations*

In total, three large-eddy simulations of free-surface flow over a backward-facing step are performed and the computational details are listed in table 2. The step height is kept at $h = 2cm$ in all cases. LES1 and LES2 correspond to the deepest ST3 and the shallowest ST1 experimental cases of Nakagawa and Nezu (1987), respectively. The spatially-averaged mean velocity U_{m1} upstream of

the step is varied across the different cases to achieve similar R_{eh} to the experiments, leading to $\mathsf{F}_{\mathsf{r}} \approx 0.2$ for all cases. Upon successful validation, another simulation, LES3, is performed featuring a greater submergence (of $S = 2$) than LES2 and at $\mathsf{R}_{\mathsf{eh}} = 5000$ and $\mathsf{F}_{\mathsf{r}} = 0.2$ with the goal to cover a wider range of relative submergence (i.e. h_2/h, where h_2 represents the water depth downstream of the step and h represents the step height) investigating the effects of relative submergence on the hydrodynamics and turbulence structure of such very shallow flows. The expansion ratio $E_r = h_2/h_1$ and the relative submergence $S = h_2/h$ are both used as non-dimensional parameter to charaterise the flow, in the following only the relative submergence S is used.

The computational domains (see figure 1 for a sketch) are $L_x = 24h$ long in the streamwise direction, which ensures the full recovery of the flow downstream of the step. The spanwise width L_y and wall-normal height L_z vary in accordance with the water depth upstream of the step, h_1, for different cases, where $L_y \geq 3h_1$, and $L_z \approx 2h_1$ to include the air phase. No-slip boundary conditions are applied at the channel bed and the step surfaces. In order to eliminate the effects of lateral flow confinement, the periodic condition is applied to the spanwise direction and hence the computational domain needs to be wide enough to not lock-in spanwise vortices which could distort the turbulence in the entire domain. Figure 2 presents u-velocity auto-correlations, R_{uu}, over half of the domain width, at a selected location in the flow (i.e. above the reattachment point). The R_{uu} curves drop to zero rather quickly, already after approximately 0.5 step height for LES2 and LES3, while in LES1 the turbulence is uncorrelated after approximately $1h$, suggesting that the chosen width of the computational domains is adequate. The computational domain is discretised using a uniform grid of $384 \times 240 \times 256$ ($= 2.4 \times 10^7$) points in the streamwise, spanwise and wall-normal directions for the deepest case and further computational details are provided in table 2. The grid has an aspect ratio of 2:2:1, i.e. the spacings in the x- and y-direction are twice that of the z-direction and the average spacings Δx^+, Δy^+, Δz^+ as provided in table 2 in dimensionless wall units, which are calculated using the time-averaged pressure gradient that drives the flow. Grid spacings of the precursor channel flows are around 5 in the horizontal directions and half of that in the wall-normal direction. Hence the LES presented here can be considered well-resolved. The near-wall grid spacing, Δz^+, downstream of the step is plotted in figure 3 for all cases. The maxima, i.e. $\Delta z^+ \approx 3.5$, are found towards the outlet where the boundary layer is nearly fully recovered and inside the recirculation zone highlighting significant backflow near the wall, and are well within the viscous sublayer and hence the simulations can be considered wall resolved. For LES1-3, fully developed turbulent flow at successive time steps is imposed at the inlet boundary by recording time series data of a certain cross-section plane from additional precursor simulations. For simplicity the free-slip condition (i.e. plane rigid lid) is applied at the water surface of the precursor channel. The precursor simulation is validated with direct numerical simulation data of turbulent channel flow at $\mathsf{R}_{\mathsf{e}}\tau = 590$ from Moser et al. (1999), however for brevity this is not shown here but can be found in Cevheri et al. (2016). Averaging of the flow quantities begins after 15 flow through periods, and continues for more than 20 further flow through periods to ensure that the turbulence statistics are well converged for all three BFS simulations. Power spectral density of the velocity fluctuation in LES1-3 are presented in figure 4, demonstrating that the LES covers a significant portion of the inertial sub-range, where energy is transferred from large-scales to small-scales over at least one decade. Energy transfer appears to be along the Kolmogorov -5/3 slope suggesting physically realistic energy transfer between scales. A sharp drop-off is noticed at very high frequencies, a result of the sub-grid scale model removing efficiently energy from the small scales.

4 Validation

Two of the LES are validated using data of the open-channel BFS flow experiments of Nakagawa and Nezu (1987), with the aim to confirm the adequacy of mesh size and boundary conditions of the

simulations and the validity of the LES. LES-computed time- and spanwise-averaged streamwise velocity profiles at different locations downstream of the step are plotted for LES1 and LES2 in figure 5 as well as for the additional simulation LES3 (bottom row). All values are normalised by the maximum time-averaged streamwise velocity, U_{max} of the upstream flow at $x/h = 0$.

Overall, LES2 (middle row) achieves very good agreement with the experimental data (open circles) in terms of streamwise velocity in all profiles. Flow acceleration above and backflow inside the recirculation zone is predicted accurately and so is the recovering boundary layer downstream of the time-averaged reattachment point. However, in the deep case (LES1), sidewall effects in the experiment may be responsible for the discrepancies between experimental data and LES1. In the experiment, the velocities were measured along the centre line of the flume which had a channel-width-to-depth-ratio of 2.8, suggesting the occurrence of not insignificant secondary flows as well as the presence of sidewall effects. In LES, periodic boundary conditions are applied in the spanwise direction and hence the experimentally-observed slightly higher streamwise velocity in the centre of the channel is not reproduced in the simulation; the discrepancy between LES and experimental profiles is particularly obvious at upstream of the step ($x/h = -1$), whereas an almost perfect match is found in the numerical work of Yoo and Paik (2020) who decided to include sidewalls to match exactly the experimental conditions of Nakagawa and Nezu (1987). Also, in the experiment a "velocity dip", i.e. the highest streamwise velocity is not located at the water surface, is observed, an indicator of secondary currents, and this velocity dip is naturally absent in the LES1. Nevertheless, LES1 reproduces the recirculation and flow reattachment accurately. The profiles of LES3, i.e. the shallowest flow, generally resemble those of LES2, however the recirculation bubble of LES3 appears to be slightly longer and the velocity gradients along the dividing streamline, i.e $\psi = 0$ (where the normalised streamfunction is defined as $\psi = \int_0^z \overline{u} dz/(U_{max}h)$), are larger in LES3 in comparison to LES2, suggesting a stronger shear layer above the recirculation zone. Further analysis of the effect of relative submergence on the flow and turbulence is provided below.

Figure 6 plots computed and measured profiles of the skin-friction coefficient, C_f, along the streamwise direction behind the step. The skin-friction coefficient is normalised by using the maximum inlet velocity as:

$$C_f = \frac{\tau_w}{\frac{1}{2}\rho U_{max}^2} \tag{5}$$

The sign of C_f divides the flow behind the step into three regions: (i) a small counter-clockwise rotating secondary recirculation bubble with positive C_f and (ii) a clockwise primary recirculation bubble expanding for approximately 5 to 7 step heights with negative C_f, depending on the relative submergence of the step followed by (iii) a recovering boundary layer with positive C_f. Overall, the distribution of C_f for all LES matches the general shape of the experimental data. However, the large negative peak observed by Jovic and Driver (1994) (BFS with a similar expansion ratio than LES1 but in a wind tunnel) is somewhat underestimated and the LES predicts larger values of C_f than the ST1 experiment. The negative peak of C_f of LES1 is only around 60% of that of Jovic and Driver (1994) and further tests with a finer grid (and substantially higher computational) cost didn't result in a considerable improvement of the peak C_f. The effect of grid resolution on the magnitude of C_f has been reported previously by Toms (2015). In their BFS-LES the C_f was generally poorly matched by the low-resolution LES; their medium-resolution LES was capable of reproducing the distribution of C_f reasonably accurately with the exception of the negative peak; the high-resolution LES on the other hand only slightly underestimates the peak C_f as observed by Jovic and Driver (1994), however the recirculation length is shortened, and exactly this behavior is also found for a finer resolution LES in the study reported here. It was shown that other factors affect significantly the negative peak of C_f including the thickness of the upstream boundary layer (Adams and Johnston, 1988), inflow conditions (Aider et al., 2007) and turbulence strength (Ötügen, 1991). Regarding the magnitude of C_f of LES2 vs ST1, the discrepancy is most likely

due to the way the skin-friction was computed. While in the LES the shear velocity is obtained directly and unambiguously from the velocity gradient in the viscous sublayer, Nakagawa and Nezu (1987) obtained their shear velocity from the van Driest curve under the assumption of the validity of Prandtl's mixing layer hypothesis in the recovering boundary layer which may or may not be applicable. The distribution of the skin-friction coefficient of LES3 is similar to the other open-channel flow cases, however LES3 features a longer recirculation zone and thus a prolonged region of negative C_f. Also, in LES3 lower skin-friction than in LES1 and LES2 is observed in the recovering boundary layer downstream of the recirculation zone.

Figure 7 plots a longitudinal profile of the wall pressure coefficient. C_p is computed from:

$$C_p = \frac{P - P_0}{\frac{1}{2}\rho U_{max}^2} \tag{6}$$

where P_0 is a reference pressure.

Overall, excellent agreement is achieved between computational and experimental results irrespective of the relative submergence. The recirculation zone features an adverse pressure coefficient up to the point of reattachment from which a strongly favourable pressure gradient follows. The C_p of the deepest flow, LES1, results in the smallest value of C_p, and with decreasing submergence the coefficient of pressure increases suggesting increased energy loss due to pressure. The LES3 profile is somewhat shifted towards the downstream direction in comparison to LES1 and LES2, which is due to its elongated recirculation zone.

Figure 8 presents profiles of streamwise velocity fluctuations and Reynolds shear stresses normalised by U_{max} at four different downstream locations (for brevity wall-normal and spanwise velocity fluctuations are not shown). For LES1, the fluctuations and stresses are generally underestimated compared to the experimental data, due to the aforementioned sidewall effect. For LES2 a convincing match between simulation and experiment is achieved, and here sidewall effects are not as pronounced than in LES1 because the experimental channel-width-to-depth ratio is 5.2, at which sidewall effects are expected to be insignificant. For all cases, the fluctuations and stresses feature a marked peak above the recirculation zone, e.g. at $x = 1h$ and $z/h \approx 1.0$, which decays only slowly towards the downstream direction while the peak of the profiles is shifted towards the bed . Even at 10 step heights downstream of the step, the Reynolds shear stress is significantly greater than near the wall. This peak suggests the generation of turbulence along the separating streamline where $\psi = 0$ (Nakagawa and Nezu, 1987) and this aspect is discussed further below. The streamwise turbulent fluctuation and shear stress profiles of LES3 are very similar to the other profiles, however another peak is observed near the water surface, i.e. $z/h \approx 2$, for the two downstream profiles ($x/h = 5$ and $x/h = 10$). At these locations, the water surface deforms due to its interaction with turbulent structures, which carry turbulent kinetic energy to the water-air interface. This interaction is elucidated in section 5.2.

Figure 9 presents computed and measured profiles of the time-averaged water surface along the streamwise direction as well as two theoretical profiles derived from energy gradient according to Nakagawa and Nezu (1987). To the authors' knowledge, the study of Nakagawa and Nezu (1987) is the only experimental open-channel BFS flow study in which the water surface was measured. In the experiment, the Froude number was similar for all configurations investigated. Therefore, there is an increase in water depth in the streamwise direction and the variation of the water surface from upstream to downstream is relatively small. Water levels were measured by a point gauge and the increase of water surface elevation for the two cases considered here, i.e. ST3 and ST1, are 0.65mm and 1mm, respectively (Nakagawa and Nezu, 1987). Figure 9 illustrates that LES1 and LES2 have successfully captured the increase in water depth in the downstream direction, and LES-predicted profiles match quite well with the measured and theoretical ones for LES1 and LES2. The flow depth starts increasing rapidly around flow reattachment and stays constant after $x/h \approx 14$ for both LES1 and 2. Not surprisingly, the shallower the flow (the lower the relative submergence),

the steeper the increase of water depth, nonetheless the increase in water depth of LES3 is nearly ten times that of LES1.

The comparisons presented suggest that the large-eddy simulations are able to reproduce with convincing accuracy first- and second-order turbulence statistics and time-averaged water surface deformation irrespective of relative submergence. The focus of the following discussions is on the hydrodynamics and turbulence of open-channel BFS flows and the interaction of step-generated large-scale turbulence on the water surface.

5 Results and Discussion

5.1 *Effect of relative submergence on turbulence statistics*

Figure 10 shows the normalised streamfunction ($\psi = \int_0^z \overline{u} dz/(U_{max}h)$) for the three BFS cases LES1 (top), LES2 (middle) and LES3 (bottom). The time- and spanwise-averaged reattachment length X_R, determined by the locations of the dividing streamline $\psi = 0$, are 5.70h, 6.08h and 7.45h for LES1, LES2 or LES3, respectively. R_{eh} of all cases presented in this paper is around 5000. The recirculation zone is clearly a function of relative submergence $S = h_2/h$, the lower S the longer the recirculation zone. LES3 exhibits a significantly longer recirculation zone than LES2, where the water surface constrains the separation-reattachment process. This is consistent with Kuehn (1980), Nadge and Govardhan (2014) and Nakagawa and Nezu (1987) who demonstrated that the reattachment length increases with an decrease in relative submergence. Noteworthy, Ötügen (1991) reported a decrease of normalized reattachment lengths with an decrease in relative submergence at constant R_{e} (based on free stream velocity and channel height upstream of the step is kept constant and therefore R_{eh} varies), albeit their wind tunnel featured a large step height compared to the height and width of the inlet channel. De Brederode (1972) and Nadge and Govardhan (2014) suggested that the channel-width-to-step-height-ratio, A_r, has a significant impact on the reattachment length, which may explain the contrasting observations between Ötügen (1991) and other studies as well as the present LES results in terms of S and X_R/h. The A_r in Ötügen (1991) is less than 10, indicating that their measured X_R/h may be affected by the sidewalls (De Brederode, 1972). In contrast the A_r in Nakagawa and Nezu (1987) is 15 and infinite in the LES and sidewall effects on X_R/h are insignificant or absent, respectively.

Interestingly, the relationship between S and X_R/h of the LES agrees well with that in open channel flow with lateral expansions of Han et al. (2020). They showed that X_R/h increases as E_r increases when $E_r < 2.86$, which is consistent with the present LES. Figure 10 also shows that a secondary bubble immediately behind the step exists in all cases. The secondary bubble extends to 1-2h in the streamwise direction and is the shortest in the shallowest BFS open-channel flow. The latter also features the strongest flow recirculation according to the contour levels.

Figure 11 presents contours of the spanwise-averaged normalised Reynolds shear stress for LES1, LES2 and LES3. The highest peaks of $-\overline{u'w'}/U_{max}^2$ are found in LES3, where the relative submergence is the lowest and hence the deceleration of the flow is the greatest. In LES3 the region of high shear stress occupies almost the entire water depth, in contrast, in the deepest flow, elevated levels of the shear stress are found near the bed and remain below $z/h = 3$. The wake (elevated levels of shear stress) in LES2 extends fairly far downstream, similar to LES3 suggesting that boundary layer recovery is slower at shallower water depth. At the water surface the wall-normal component approaches zero so naturally the shear stress approaches zero at the water surface in all cases.

Figure 12 depicts spanwise-averaged normal Reynolds stresses normalised by U_{max}^2 in streamwise, spanwise and wall-normal directions. An identical sudden increase in the respective values in all directions behind the step is observed due to the sudden deceleration of the flow and the presence of the shear layer. Similarly to the shear stress, the highest normal stresses are found in the lowest submergence case, LES3. The highest velocity fluctuations are observed in the streamwise direction,

which carries the largest amount of kinetic energy. The spanwise velocity fluctuations are larger than those in the wall-normal direction, particularly for LES3. The flow structures can expand in the spanwise direction whereas they are quite a constraint in the wall-normal direction and hence the velocity fluctuations in the spanwise direction carry more turbulent kinetic energy. This has also been reported in Le et al. (1997) for their wind tunnel BFS flow.

Figure 13 presents contours of the spanwise-averaged normalised turbulent kinetic energy TKE/U_{max^2} for the three simulations ($TKE = 0.5(\overline{(u')^2} + \overline{(v')^2} + \overline{(w')^2})$). The largest values of TKE are found in LES3, and the lowest in LES1, where the region of elevated levels of TKE are concentrated near the bed, very similar to the turbulent shear stress. The turbulence in LES3 interacts with the water surface, and distinct elevated levels of TKE are observed immediately after the rapid increase of the water surface, i.e. after $x/h \approx 6$. Elevated near-surface turbulence is also noticed in LES2, however a bit further downstream than in LES3, i.e. after $x/h \approx 13$. Large-scale turbulence structures are generated in the shear layer just downstream of the step, which are then advected upwards towards the water surface where they break up and deform the surface. The elevated levels of TKE at the water surface are the signature of the interaction of the turbulence structures with the water surface.

The transport equation for the turbulent kinetic energy is given as:

$$\frac{\partial K}{\partial t} = -\overline{u_i}\frac{\partial K}{\partial x_i} - \frac{1}{\rho}\frac{\partial \overline{u_i' p'}}{\partial x_i} - \frac{1}{2}\frac{\partial \overline{u_j' u_j' u_i'}}{\partial x_i} - \overline{u_i' u_j'}\frac{\partial \overline{u_i}}{\partial x_j} + \nu\frac{\partial^2 K}{\partial x_j^2} - \epsilon \tag{7}$$

From left to right, the terms refer to local derivative (equals zero in a time-averaged field), *Advection*, *Pressure Transport*, *Turbulent Transport*, *Production*, *Viscous Diffusion* and *Dissipation*. Here, K is the turbulent kinetic energy, and its spanwise-averaged distribution in the domain is plotted in figure 13. The pressure transport and the viscous diffusion are one (pressure transport) or two (viscous diffusion) orders of magnitude lower than the other terms so they are not shown for brevity.

The distributions of the main terms of the TKE transport equation are presented in figures 14 to 17. All cases, exhibit very similar contributions to the TKE transport equation, with LES1 having the lowest magnitudes of the respective transport terms and LES3 the highest. In general, all terms have large values just downstream of the step which is where the turbulent kinetic energy is greatest.

Figure 14 presents the first term on the right hand side of equation 7 and the highest values of the transport of TKE by the mean velocity are found downstream of the step where the gradient of the TKE is high. There is generally an upward trend in the TKE transport as a result of relative submergence. The *Transport* is negative for increasing TKE and positive for decreasing TKE. The flow in the spanwise direction is zero and hence $\overline{v}(\partial K/\partial y)$ is zero. The $\overline{w}(\partial K/\partial z)$ term is mainly responsible for the positive advective transport within the reattachment area while each of the terms $\overline{u}(\partial K/\partial x)$ and $\overline{w}(\partial K/\partial z)$ contribute around 50% to the negative advective transport that originates at the step.

Figure 15 presents contours of the third term on the right hand side of equation 7, i.e. the transport of TKE by turbulent fluctuations. Peaks of positive turbulent transport are on the edges of the shear layer, i.e. where the gradients of TKE are greatest and turbulent fluctuations are significant. In between is a region of large negative turbulent transport and areas coincide with very high levels of the shear stress $-u'w'$ which is dominated by quadrant two and four events, i.e. negative streamwise fluctuations and positive wall-normal fluctuations (Q2) and vice versa (Q4).

Figure 16 shows contours of the production of TKE by shear and the peaks of the *Production* are the result of high levels of the shear stress and a positive velocity gradient in the wall-normal direction, i.e. the dominance of $\overline{u'w'}(\partial\overline{u}/\partial z)$. There are very small patches of negative *Production* near the wall, i.e. where the flow recirculates (i.e. negative velocity gradient), however there is

very little shear near the wall because the velocity gradient is weak and the shear stress is small compared to the high values inside the shear layer (around the dividing streamline). Turbulent production is in general the term that has the largest magnitude of all the terms. Noteworthy is the fact that turbulence is produced over the entire water depth in LES3, whilst it is confined to a thin band near the lower wall (and barely above the step height) in LES1.

Figure 17 shows contours of ϵ, i.e. the dissipation of TKE and the largest values are on the fringe of the shear layer. The dissipation is an (almost) equal counterpart to the shear production, i.e. generally of the same order of magnitude but with opposite sign. Large values of the *Dissipation* are found near the flow reattachment zone which is where gradients of the turbulent fluctuations are large and in the shear layer. The dissipation of turbulent kinetic energy is limited to the lower third of the flow depth in the deep case, however is observed throughout the water depth in LES2 and LES3. High gradients of the turbulent fluctuations reach the water surface shortly after flow reattachment in LES3, whereas this takes place a bit further downstream in the LES2 case.

In general, the magnitudes of *Advection*, *Turbulent Transport*, *Production* and *Dissipation* are all in reasonable agreement with the DNS of Le et al. (1997) and the experimental study of Piirto et al. (2003).

The state of turbulence in a flow can be quantified using eigenvalues of the stress tensor, here obtained at selected locations (a, b, c, d, e, f as denoted in figure 18 (a) and then plotted inside the Lumley triangle in figure 18 (b)). Only one set of points, sampled in location "d", is found near the "oblate" side of the triangle. The location is just above the mean flow reattachment point and here the turbulence attains a disc form, i.e. structures are dominated by fluctuations in the streamwise and spanwise directions due to the proximity of the wall. Most of the other points are found towards the right hand side of the triangle, where turbulence is due to vortex stretching and the turbulence state is very similar for all three flows along the dividing streamline as well as in the recirculation zone. The flow inside the recirculation zone tends towards isotropic however due to the quasi-2d geometry of the flow there is a bi-directionality. Similarly, near the water surface, the turbulence state of the three flows is similar, however the turbulence structures of LES3 are more energetic (higher TKE) and deform more the water surface than LES1 and LES2 and hence structures appear to be able to maintain a prolate-shape instead of being forced to 2-component turbulence by the water-air boundary. The biggest deviation in the turbulence structure between LES1 and LES2/LES3 is observed at location "e", i.e. at mid-depth downstream of the recirculation zone. Whilst in LES2 and LES3 the points lie towards the right, i.e. the prolate (elongated, stretched) side of the triangle, the point of LES1 lies towards the oblate side, suggesting that the flow of LES1 at half depth appears more isotropic however with a limited amount of vertical fluctuations as the turbulence structures are approaching the water surface. In contrast, the flow at half depth in LES2 and LES3 is still inside the turbulent wake due to the limited water depth and distinct longitudinal vortex stretching takes place, almost until 1-component turbulence is attained.

5.2 *Step-generated coherent structures and water surface deformation*

The location of the water surface affects the flow separation-reattachment process downstream of the step and large-scale turbulence structures are generated in the shear layer downstream of the step. These are then advected towards the water surface where they break-up and deform the surface. This section focuses on discussing the interaction between step-generated coherent turbulence structures and water surface deformation.

Figure 19 visualises the instantaneous water surface for all three open-channel BFS cases. The water surface increase from upstream to downstream is appreciated in these plots. It also shows that the lower the relative submergence, the more significant the water surface deforms, especially when comparing LES1 with LES3. In LES1 only a few mild water surface waves are observed whereas in LES3 clear deformations due to the turbulence underneath the water surface are noticed.

Figure 20 presents isosurfaces of the Q-criterion and contours of the normalised instantaneous vorticity magnitude in a longitudinal plane at an arbitrary instant in time for the three free-surface flows. The images show the features of the coherent turbulence generation (due to the Kelvin–Helmholtz instabilities) in the shear layer of the instantaneous recirculation and their transport (advection) by the ambient flow. The interaction of a substantial amount of coherent flow structures with the water surface is visible in LES3, whereas fewer vortices are observed in LES1 and LES2. In LES3 the vortices reach the surface approximately ten step heights downstream of the step, to be identified by an area of high vorticity at the water surface at the instant depicted. In LES1 the vortices generated at the step don't appear to be reaching the water surface over the distance shown in the figures, whilst in LES2 some interaction of vortices with the water surface occurs, albeit further downstream than in LES3, at $x/h \approx 15$, and with less vorticity/strength. These visualisations are clearly reflected in the water surface plots of figure 19.

Coherent turbulence structures are depicted better with isosurfaces of pressure fluctuations in figure 21 (only LES2 is shown for brevity). Various types of turbulence structures can be identified. Near the step there are rollers, i.e. quasi 2D structures that rotate about the y-axis, which are the result of flow separation and shear layer roll-up. These structures are advected with the ambient flow, generally along the dividing streamline, and their fate varies between break-down, tearing, pairing and amalgamation (Hu et al., 2016). Some structures are transported towards the water surface during low momentum ejections whereas others travel towards the bed as the flow expands. The largest turbulence structures are found past the mean reattachment point, here, the so-called "kolk-boils" emerge from near the bed. Kolk-boils represent coherent structures associated with a strong upward motion and effectively transport low momentum from the bed to the water surface (Rodi et al., 2013). The kolk-boils generally appear to be taking the shape of inclined horseshoe vortices, probably due to up-lifting and stretching of rollers. Other vortices found in the shear layer vary in size, smaller ones are remains of a broken-up roller, others are legs of torn horseshoe vortices and larger ones are amalgamated or paired vortices and they are elongated due to shear layer stretching.

Based on the observations made from figures 19, 20 and 21, it is worthy to highlight the necessity of using a (deforming) free-surface boundary condition rather than a rigid-lid-free-slip boundary condition. Step-generated coherent structures carry a significant amount of energy to the water surface which was are seen to generate water surface boils and this is most pronounced in the shallowest case, LES3. If a rigid-lid-free-slip condition was imposed, these energetic turbulence structures would "bounce off" from the rigid lid, the normal (to the water surface) velocity fluctuations would be set to zero and the energy carried by the coherent structures would be redistributed (rather artificially) into streamwise and spanwise normal stresses, leading to an over-prediction of these stresses close to the water surface (Stoesser, 2014). A deforming water surface on the other hand produces secondary vorticity, which alters the near-surface turbulence (Shen et al., 1999).

In order to track the generation and fate of shear-layer-induced turbulent structures behind the step, auto-correlation functions are obtained. Here the spanwise auto-correlation function, R_{vv} is chosen, which is calculated as:

$$R_{\mathrm{vv}}(x_\mathrm{r}, z_\mathrm{r}, \Delta x, \Delta z) = \frac{\sum^{t} v'(x_\mathrm{r}, z_\mathrm{r}, t) v'(x_\mathrm{r}+\Delta x, z_\mathrm{r}+\Delta z, t)}{\left(\sum^{t}[v'(x_\mathrm{r}, z_\mathrm{r}, t)]^2\right)^{0.5} \left(\sum^{t}[v'(x_\mathrm{r}+\Delta x, z_\mathrm{r}+\Delta z, t)]^2\right)^{0.5}} \tag{8}$$

For brevity only contours of R_{vv} are shown, where contours of R_{uu} and R_{ww} show exactly the same features. Four reference locations are chosen along the time-averaged dividing streamline ($\psi = 0$) indicted in figure 22. Velocity signals are collected at every fourth grid point in the x-z plane and at a few planes in the y-direction, covering 280 flow-throughs. Figure 22 presents contours of

R_{vv}, here for LES2, clearly illustrating that coherent flow structures originate at various locations along the recirculation zone, owing to the intermittency of the flow and the spatial variability of flow separation and reattachment. At each of the chosen locations, the trajectory of the shed vortices is approximately 45 degrees. It is interesting to observe that the later the vortex travels upwards, the longer it maintains its coherence. The grey area around the reference point at the mean reattachment location, Figure 22 (d), is the largest and extends the furthest in the streamwise direction. This is the afore-mentioned kolk-boil vortex which has been found to be dominant in such flows.

Figure 23 presents contours of R_{vv} for the deep flow, LES1, and the shallow flow, LES3. Similar observations can be made for LES3, however the contours of R_{vv} remain dark grey and in a narrow envelope until the water surface is reached whereas in LES1, R_{vv} shows the vortices lose coherence quickly and the turbulence is spread over a wider area. When using a reference point closer to the step, the values of R_{vv} drop below zero before the water surface is reached, corroborating the observations of LES2 that structures are less coherent and energetic when being shed closer to the step. Figure 23 provides quantitative evidence that step- (or better shear-layer) induced turbulence structures have limited impact on the water surface at high relative submergence compared to those at low relative submergence, which is also reflected in the water surface plots of figure 19.

The behaviour of the shear-layer-induced coherent structures visualised and discussed above can also be appreciated by the dominant frequency in the frequency spectra of velocity signals at $x = 5h, z = 1h$ (which corresponds to the reference location in figure 22 (c) and figure 23) plotted in figure 4. A significant peak (marked with an arrow in figure 4) is observed at low frequency for all cases, corresponding to a Strouhal number ($\mathsf{s_t} = fh/U_{max}$) of 0.074, 0.045 and 0.023 for LES1, LES2 and LES3, respectively. The Strouhal numbers found here are comparable to those previously reported by Le et al. (1997) and Wee et al. (2004), and quantify the oscillation of the recirculation zone (the streamwise and vertical movement of the shear layer in time) and therefore the shedding of the shear-layer-induced coherent structures.

6 Conclusions

Large-eddy simulations (LES) of free-surface flows over a backward facing step have been carried out for various relative submergences, ranging from deep to shallow flows. In a first step, the LES method has been validated using experimental data confirming the adequacy of the selected discretisation schemes, the mesh size, subgrid-scale model as well as boundary conditions. Comparisons of LES-computed first and secondary turbulence statistics, as well as distributions of the coefficients of friction and pressure, showed convincing agreements with measured data. The data of two open-channel flow experiments included mean water surface deformation for the deep (LES1) and a medium-depth (LES2) flow over a step and the LES reproduced these deformations rather well. Upon successful validation, a shallow flow has been added to the analysis and the mean streamfunction plots revealed that the recirculation increases with the reduction of water depth (i.e. decrease in relative submergence). As the flow separates from the edge of the step, a strong shear layer is formed around the dividing streamline and the shallower the flow (i.e. the lower the relative submergence), the stronger this shear layer. This is also manifested in the contours of the turbulent shear stress or the turbulent kinetic energy (TKE), respectively. The quantification of the main contributing terms of the transport of turbulent kinetic energy revealed that the two dominating terms are shear production and TKE dissipation, both terms attain their maxima (approximately equal in magnitude but of opposite sign) in the shear layer behind the step. Turbulent and advective transport are both found to be significant around the dividing streamline and are of similar magnitude to the production and dissipation. A Reynolds stress tensor analysis, including the Lumley triangle, pointed out areas of turbulence anisotropy in this shear layer together with the obligatory vortex stretching near wall and water surface boundaries. The area near the mean

reattachment is characterised by two-component oblate turbulence structures, as separated flow splats onto the bed. The three instantaneous flows have been visualised with isosurfaces of the Q-criterion and pressure fluctuations, and these have revealed the presence of rollers initially (as the shear layer rolls up) which deform into horseshoe or hairpin-type structures, the most prominent one springing off the shear layer close to flow reattachment, known as the kolk-boil vortex. However, two-dimensional auto-correlations in space have demonstrated that such vortices can originate at (almost) any location along the dividing streamline, yet the one shed closest to flow attachment appears to feature the greatest coherence. These vortices are advected towards the water surface where they deform the water surface being most pronounced for the shallowest flow, whereas the turbulence-structure-water-surface interaction is quite weak for the deep case.

Acknowledgments

All simulations were performed on UCL's supercomputer Kathleen.

Funding

The work presented in this paper is supported by the EPSRC under project number EP/R022135/1. The third author is a postdoctoral fellow sponsored by EP/R022135/1 whereas the first author has been funded by UCL's Department of Civil, Environmental and Geomatic Engineering.

Notation

A_r = channel-width-to-step-height-ratio (–)
C_f = skin-friction coefficient (–)
C_p = pressure coefficient (–)
E_r = expansion ratio (–)
$\mathsf{F_r}$ = Froude number (–)
f = frequency (Hz)
$\boldsymbol{f}$ = volume force from immersed boundary points (N m^{-3})
$\boldsymbol{g}$ = gravitational acceleration (m s^{-2})
h = step height (m)
h_1 = upstream depth (m)
h_2 = downstream depth (m)
K = turbulent kinetic energy (m^2 s^{-2})
L_x = computational streamwise length (m)
L_y = computational spanwise width (m)
L_z = computational wall-normal height (m)
p = pressure (Pa)
$\mathsf{R_e}$ = bulk Reynolds number (–)
$\mathsf{R_{eh}}$ = step height Reynolds number (–)
$\mathsf{R_e}\tau$ = friction Reynolds number (–)
R_{uu} = u-velocity auto-correlation (–)
R_{vv} = v-velocity auto-correlation (–)
S = submergence (–)
$\mathsf{S_t}$ = Strouhal number (–)
t = times (s)
$\boldsymbol{u}$ = filtered resolved velocity field (m s^{-1})
$\overline{u}$ = time-averaged streamwise velocity (m s^{-1})
$-\overline{u'w'}$ = time-averaged Reynolds shear stress (m s^{-2})
U_{max} = maximum time-averaged streamwise velocity (m s^{-1})
U_{m1} = upstream spatially-averaged mean velocity (m s^{-1})
U_{m2} = downstream spatially-averaged mean velocity (m s^{-1})
X_R = reattachment length (m)
Γ = interface between gas and liquid domains (–)
ϵ = turbulent kinetic energy dissipation (m^2 s^{-3})
ν = kinematic viscosity (m^2 s^{-1})
ρ = density of liquid (kg m^{-3})
τ_{SGS} = sub-grid scale stress tensor (–)
τ_w = wall shear stress (Pa)
ϕ = level set distance function (–)
ψ = normalised streamfunction (–)
Ω_{gas} = gas domain (–)
Ω_{liquid} = liquid domain (–)

ORCID

QIANYU LUO https://orcid.org/0000-0002-2967-0599
THORSTEN STOESSER https://orcid.org/0000-0001-8874-9793
ZHIHUA XIE https://orcid.org/0000-0002-5180-8427

References

Adams, E. & Johnston, J. (1988). Effects of the separating shear layer on the reattachment flow structure part 2: Reattachment length and wall shear stress. *Experiments in Fluids*, *6*(7), 493–499, https://doi.org/10.1007/BF00196511.

Aider, J.-L., Danet, A., & Lesieur, M. (2007). Large-eddy simulation applied to study the influence of upstream conditions on the time-dependant and averaged characteristics of a backward-facing step flow. *Journal of Turbulence*, *8*, N51, https://doi.org/10.1080/14685240701701000.

Babarutsi, S., Ganoulis, J., & Chu, V. (1989). Experimental investigation of shallow recirculating flows. *Journal of Hydraulic Engineering*, *115*(7), 906–924, https://doi.org/10.1061/(ASCE)0733-9429(1989)115:7(906).

Cevheri, M., McSherry, R., & Stoesser, T. (2016). A local mesh refinement approach for large-eddy simulations of turbulent flows. *International Journal for Numerical Methods in Fluids*, *82*, 261–285, https://doi.org/10.1002/fld.4217.

Chorin, A. J. (1968). Numerical solution of the navier-stokes equations. *Mathematics of computation*, *22*(104), 745–762.

Chua, K., Fraga, B., Stoesser, T., Hong, S., & Sturm, T. (2019). Effect of bridge abutment length on turbulence structure and flow through the opening. *Journal of Hydraulic Engineering*, *145*(6), 04019024, https://doi.org/10.1061/(ASCE)HY.1943-7900.0001591.

De Brederode, V. (1972). Three-dimensional effects in nominally two-dimensional flows. *PhD thesis, Imperial College London*.

Friedrich, R. & Arnal, M. (1990). Analysing turbulent backward-facing step flow with the lowpass-filtered navier-stokes equations. *Journal of Wind Engineering and Industrial Aerodynamics*, *35*, 101–128, https://doi.org/10.1016/0167-6105(90)90212-U.

Han, L., Mignot, E., & Riviere, N. (2017). Shallow mixing layer downstream from a sudden expansion. *Journal of Hydraulic Engineering*, *143*(5), 04016105, https://doi.org/10.1061/(ASCE)HY.1943-7900.0001274.

Han, L., Riviere, N., Chatelain, M., & Mignot, E. (2020). Recirculation zone downstream lateral expansions of open channel flow. *Physics of Fluids*, *32*(11), 115119, https://doi.org/10.1063/5.0018343.

Hu, R., Wang, L., & Fu, S. (2016). Investigation of the coherent structures in flow behind a backward-facing step. *International Journal of Numerical Methods for Heat & Fluid Flow*, https://doi.org/10.1108/HFF-09-2015-0403.

Jovic, S. & Driver, D. M. (1994). Backward-facing step measurements at low reynolds number, re (sub h)= 5000. *NASA Technical Memorandum 108807*.

Kara, S., Stoesser, T., & Sturm, T. (2015a). Free-surface versus rigid-lid les computations for bridge-abutment flow. *Journal of Hydraulic Engineering*, *141*(9), 04015019, https://doi.org/10.1061/(ASCE)HY.1943-7900.0001028.

Kara, S., Stoesser, T., Sturm, T., & Mulahasan, S. (2015b). Flow dynamics through a submerged bridge opening with overtopping. *Journal of Hydraulic Research*, *53*(2), 186–195, https://doi.org/10.1080/00221686.2014.967821.

Kuehn, D. M. (1980). Effects of adverse pressure gradient on the incompressible reattaching flow over a rearward-facing step. *AIAA journal*, *18*(3), 343–344, https://doi.org/10.2514/3.50765.

Le, H., Moin, P., & Kim, J. (1997). Direct numerical simulation of turbulent flow over a backward-facing step. *Journal of fluid mechanics*, *330*, 349–374, https://doi.org/10.1017/S0022112096003941.

Liu, Y., Stoesser, T., & Fang, H. (2022a). Effect of secondary currents on the flow and turbulence in partially-filled pipes. *Journal of Fluid Mechanics*, *938*, A16, https://doi.org/doi:10.1017/jfm.2022.141.

Liu, Y., Stoesser, T., & Fang, H. (2022b). Impact of turbulence and secondary flow on the water

surface in partially-filled pipes. *Physics of Fluids*, *34*, 035123.
Liu, Y., Stoesser, T., Fang, H., Papanicolaou, A., & Tsakiris, A. G. (2017). Turbulent flow over an array of boulders placed on a rough, permeable bed. *Computers & Fluids*, *158*, 120–132.
McSherry, R., Chua, K., & Stoesser, T. (2017). Large eddy simulation of free-surface flows. *Journal of Hydrodynamics*, *29*(1), 1–12, https://doi.org/10.1016/S1001-6058(16)60712-6.
McSherry, R., Stoesser, T., & Chua, K. (2018). Free surface flow over square bars at intermediate relative submergence. *Journal of Hydraulic Research*, *56*(6), 825–843, https://doi.org/10.1080/00221686.2017.1413601.
Moser, R. D., Kim, J., & Mansour, N. N. (1999). Direct numerical simulation of turbulent channel flow up to re τ= 590. *Physics of fluids*, *11*(4), 943–945, https://doi.org/10.1063/1.869966.
Nadge, P. M. & Govardhan, R. (2014). High reynolds number flow over a backward-facing step: structure of the mean separation bubble. *Experiments in fluids*, *55*(1), 1657, https://doi.org/10.1007/s00348-013-1657-5.
Nakagawa, H. & Nezu, I. (1987). Experimental investigation on turbulent structure of backward-facing step flow in an open channel. *Journal of Hydraulic Research*, *25*(1), 67–88, https://doi.org/10.1080/00221688709499289.
Nicoud, F. & Ducros, F. (1999). Subgrid-scale stress modelling based on the square of the velocity gradient tensor. *Flow, turbulence and Combustion*, *62*(3), 183–200, https://doi.org/10.1023/A:1009995426001.
Nikora, V., et al. (2019). Friction factor decomposition for rough-wall flows: theoretical background and application to open-channel flows. *Journal of Fluid Mechanics*, *872*, 626–664, https://doi.org/10.1017/jfm.2019.344.
Osher, S. & Sethian, J. A. (1988). Fronts propagating with curvature-dependent speed: algorithms based on hamilton-jacobi formulations. *Journal of computational physics*, *79*(1), 12–49, https://doi.org/10.1090/S0025-5718-1968-0242392-2.
Ötügen, M. (1991). Expansion ratio effects on the separated shear layer and reattachment downstream of a backward-facing step. *Experiments in fluids*, *10*(5), 273–280, https://doi.org/10.1007/BF00202460.
Ouro, P., Fraga, B., Lopez-Novoa, U., & Stoesser, T. (2019). Scalability of an Eulerian-Lagrangian large-eddy simulation solver with hybrid MPI/OpenMP parallelisation. *Computers & Fluids*, *179*, 123–136, https://doi.org/10.1016/j.compfluid.2018.10.013.
Piirto, M., Saarenrinne, P., Eloranta, H., & Karvinen, R. (2003). Measuring turbulence energy with piv in a backward-facing step flow. *Experiments in fluids*, *35*(3), 219–236, https://doi.org/10.1007/s00348-003-0607-z.
Rodi, W., Constantinescu, G., & Stoesser, T. (2013). *Large-eddy simulation in hydraulics*. Crc Press.
Shen, L., Zhang, X., Yue, D. K., & Triantafyllou, G. S. (1999). The surface layer for free-surface turbulent flows. *Journal of Fluid Mechanics*, *386*, 167–212, https://doi.org/10.1017/S0022112099004590.
Stoesser, T. (2014). Large-eddy simulation in hydraulics: Quo vadis? *Journal of Hydraulic Research*, *52*(4), 441–452, https://doi.org/10.1080/00221686.2014.944227.
Stoesser, T., McSherry, R., & Fraga, B. (2015). Secondary currents and turbulence over a non-uniformly roughened open-channel bed. *Water*, *7*(9), 4896–4913, https://doi.org/10.3390/w7094896.
Sussman, M., Smereka, P., Osher, S., et al. (1994). A level set approach for computing solutions to incompressible two-phase flow. *Journal of Journal of Computational Physics*, *114*(1), 146–159, https://doi.org/10.1006/jcph.1994.1155.
Toms, B. (2015). Large-eddy simulation of flow over a backward facing step: assessment of inflow boundary conditions, eddy viscosity models, and wall functions. *Journal of Applied Mechanical Engineering*, *4*, 169, https://doi.org/10.4172/2168-9873.1000169.
Wee, D., Yi, T., Annaswamy, A., & Ghoniem, A. F. (2004). Self-sustained oscillations and vortex

shedding in backward-facing step flows: Simulation and linear instability analysis. *Physics of Fluids*, *16*(9), 3361–3373, https://doi.org/10.1063/1.1773091.

Yoo, D. & Paik, J. (2020). Numerical study on a turbulent backward-facing step flow in open-channel. *Proceedings of the 22nd IAHR APD Congress (Sapporo, 2020)*.

Table 1 Flow conditions of the two experiments used for validation of the LES method

Case	*Type*	h_2/h_1	h_2/h	R_{eh}	F_r
Nakagawa and Nezu (1987)-ST1	Exp	1.53	2.9	4334	0.22
Nakagawa and Nezu (1987)-ST3	Exp	1.23	5.3	5448	0.19

Table 2 Computational details of the three LES simulations

LES	Corresponding Experiment	h_2/h	R_{eh}	F_r	Domain size	Grid Points	Grid Spacing
1	ST3	5.3	5180	0.21	24h×15h×8h	384×240×256	5.05×5.05×2.53
2	ST1	3.0	4380	0.19	24h×6h×4h	384×96×128	4.40×4.40×2.20
3	-	2.0	5000	0.20	24h×6h×3h	384×96×96	4.27×4.27×2.14

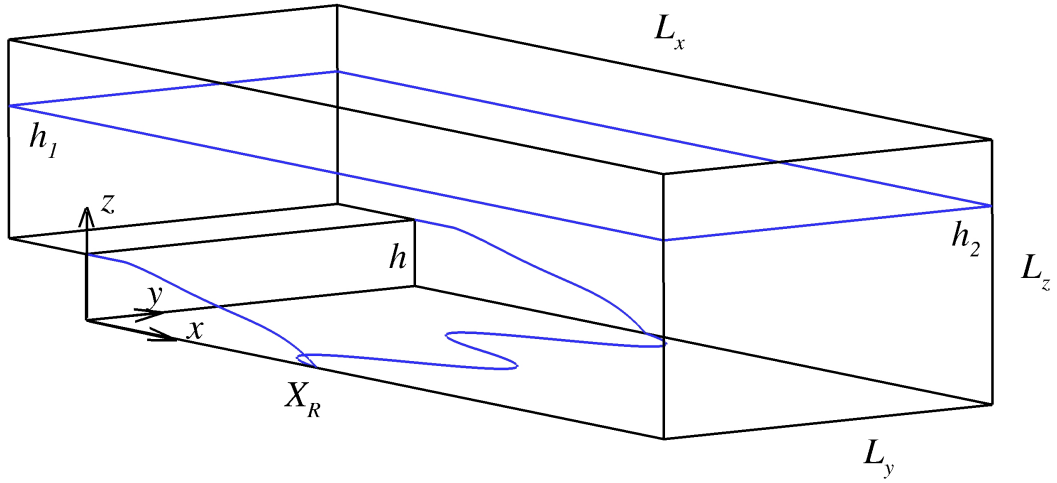

Figure 1 Sketch of computational setup

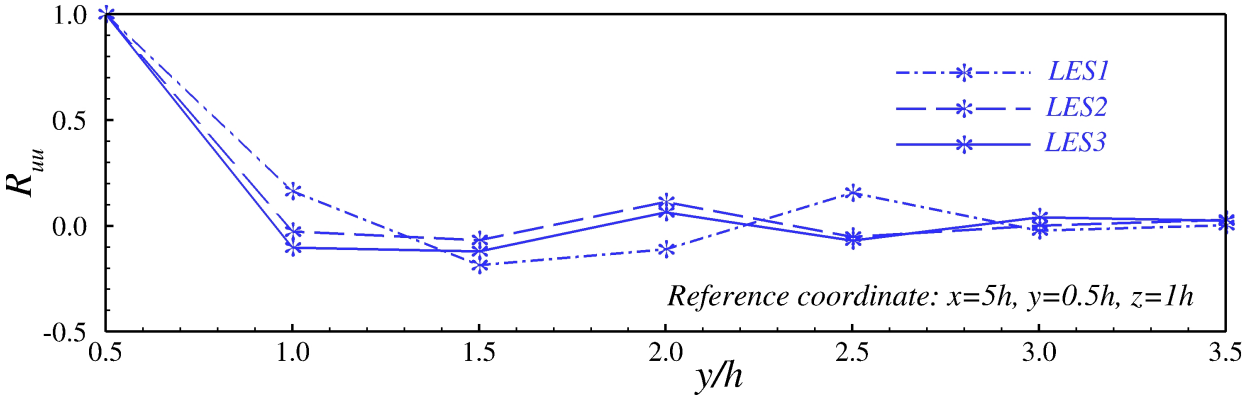

Figure 2 Auto-correlation function of the streamwise velocity fluctuation as a function of distance in spanwise direction. Symbols denote the locations where the time series are recorded and gathered in spanwise

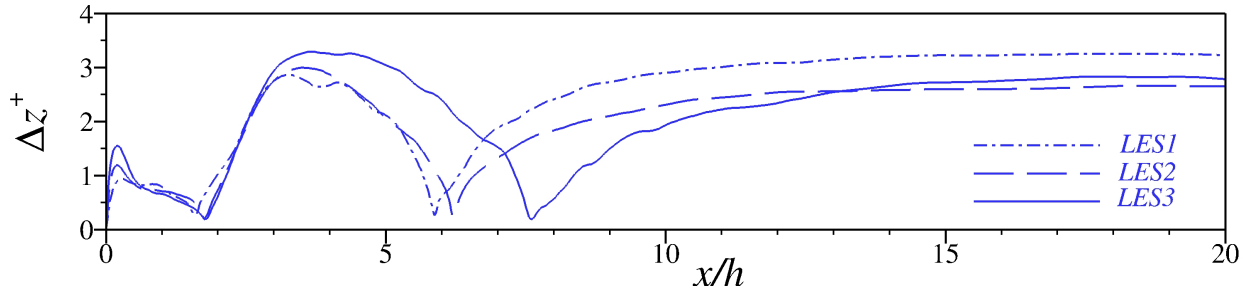

Figure 3 Wall-normal grid spacing of the three LES simulations

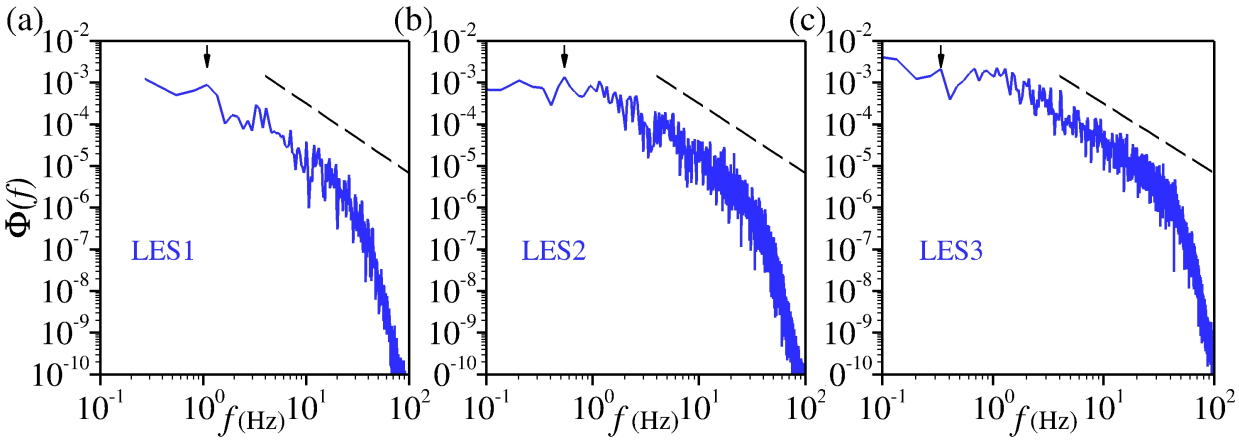

Figure 4 Power spectral density of streamwise velocity fluctuations obtained at x=5h, y=0.5h, z=1h. Dashed line exhibits Kolmogorov's slope (-5/3); Arrows indicate the frequency of the shedding of the shear-layer-induced coherent structures

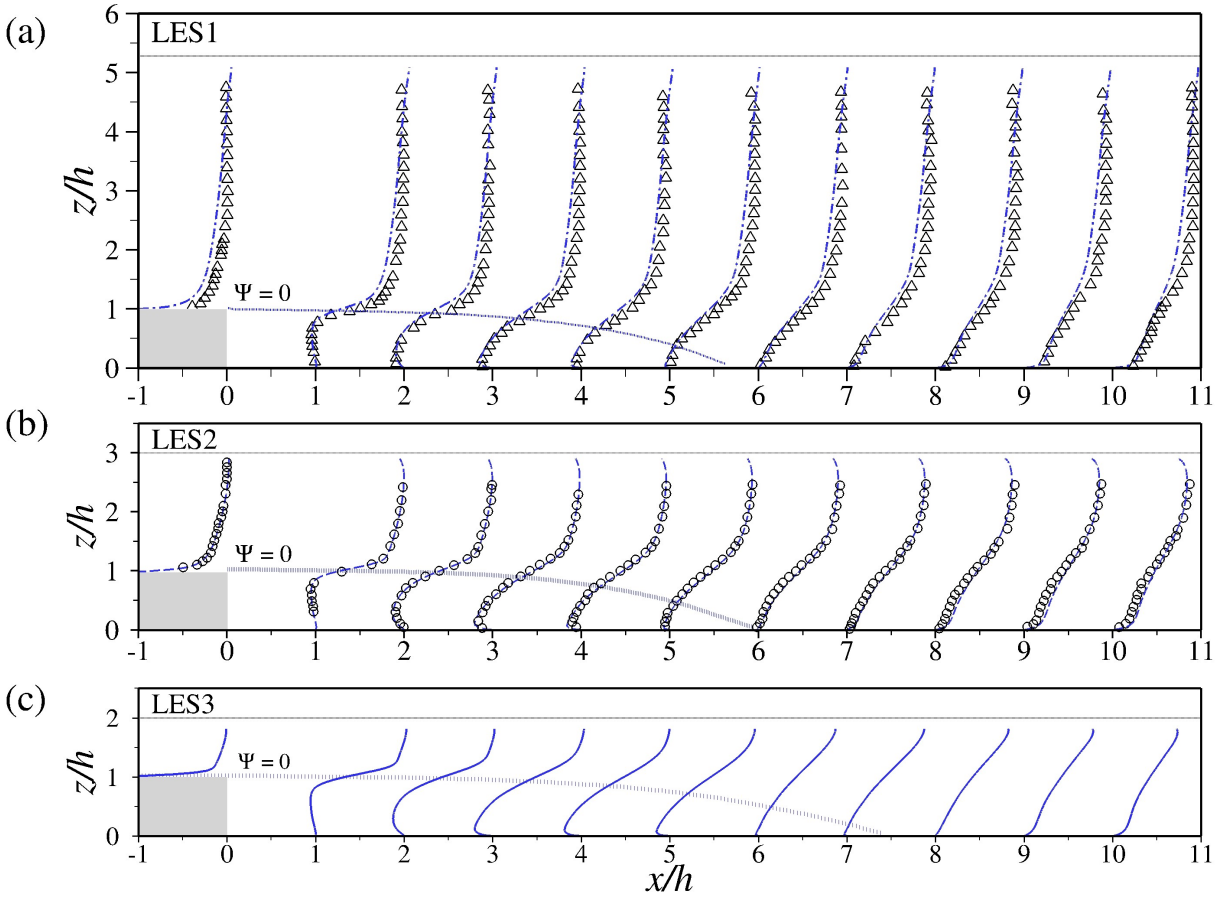

Figure 5 Profiles of the time- and spanwise-averaged streamwise velocity at various locations along the streamwise direction. blue lines: LES; open symbols: experimental data

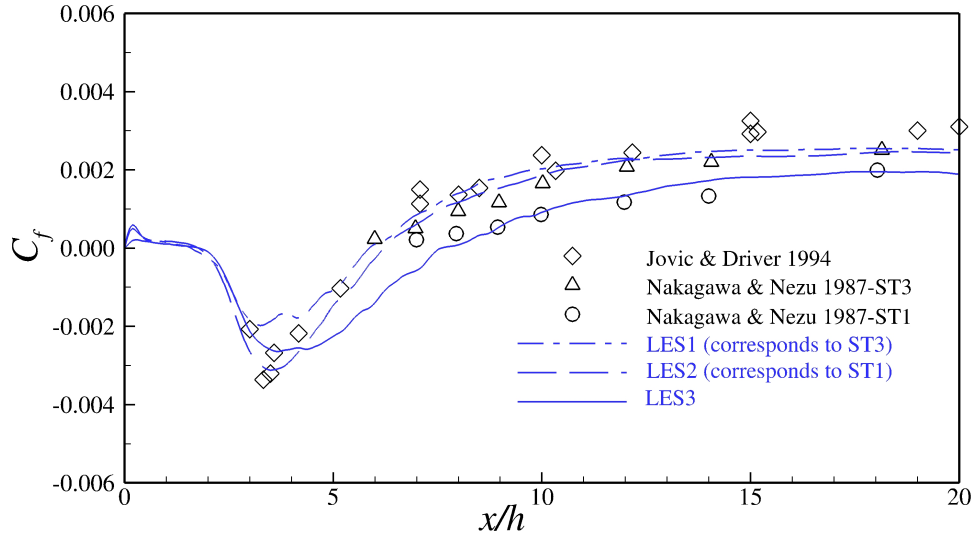

Figure 6 Wall skin-friction coefficient as a function of streamwise distance from the step

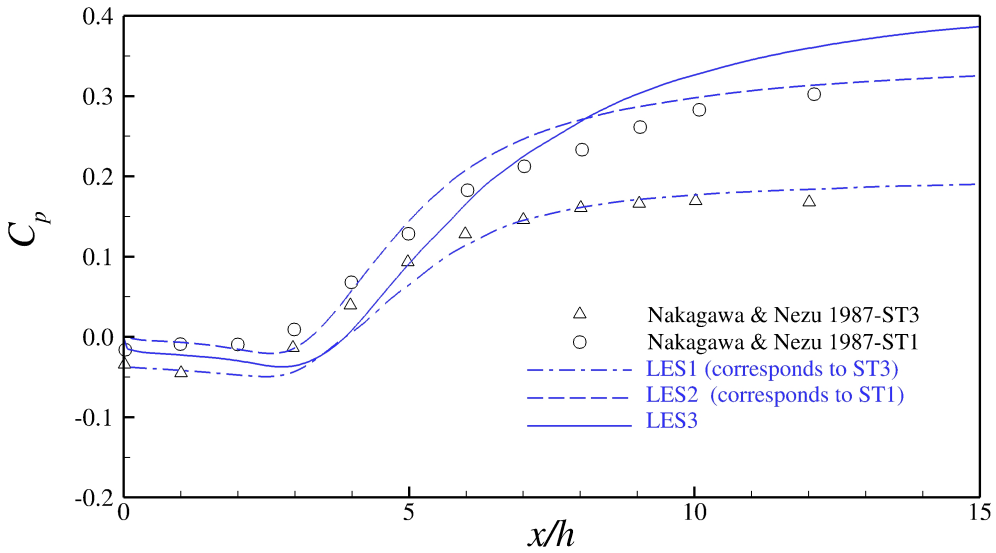

Figure 7 Pressure coefficient as a function of streamwise distance from the step

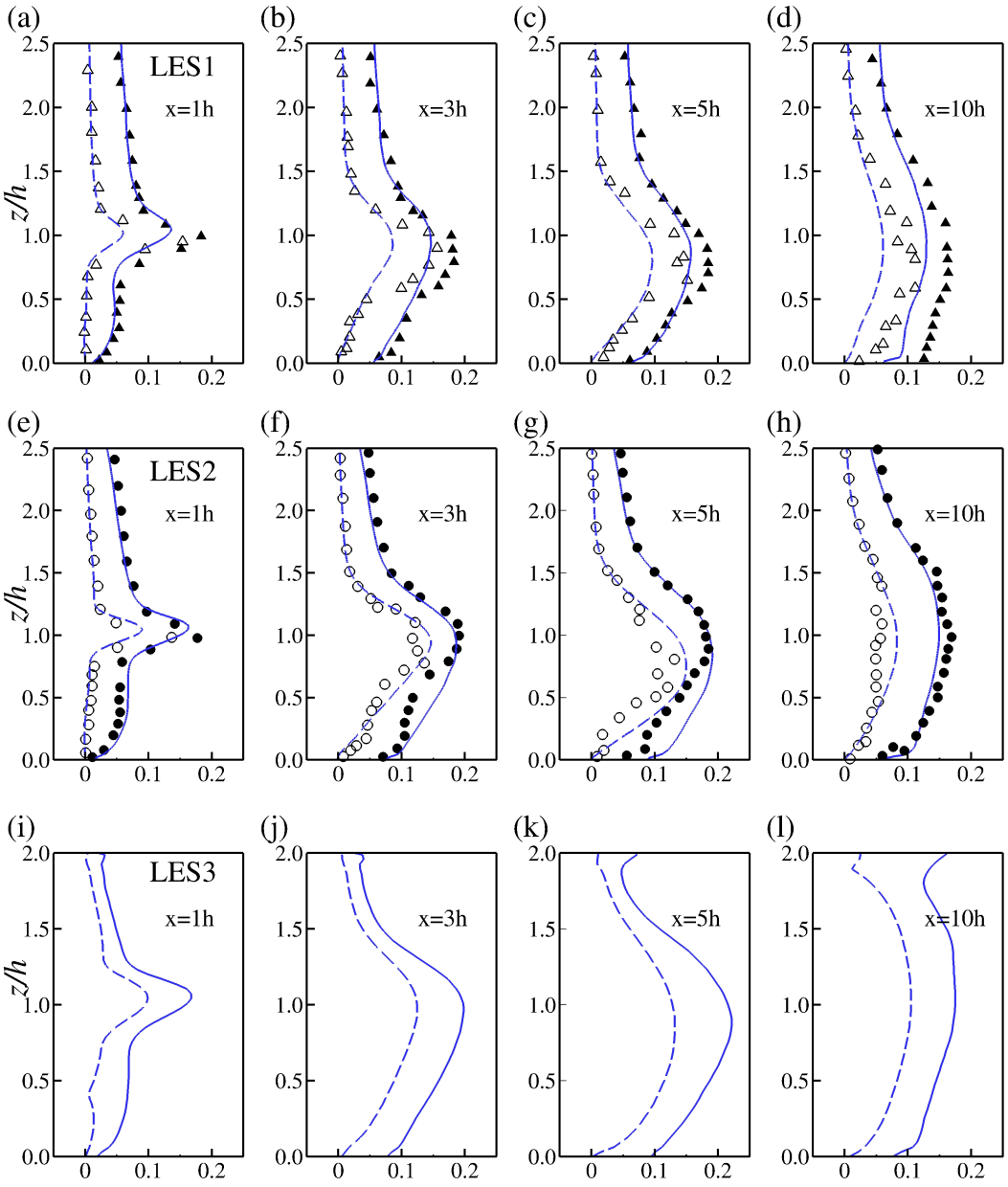

Figure 8 Profiles of normalised turbulence intensity ($\overline{u'}/U_{max}$) and shear stress ($-\overline{u'w'}/U_{max}^2$); Solid blue lines: LES $\overline{u'}/U_{max}$; dashed blue lines: LES $-\overline{u'w'}/U_{max}^2 \times 10$; closed symbols: experimental $\overline{u'}/U_{max}$; open symbols: experimental $-\overline{u'w'}/U_{max}^2 \times 10$

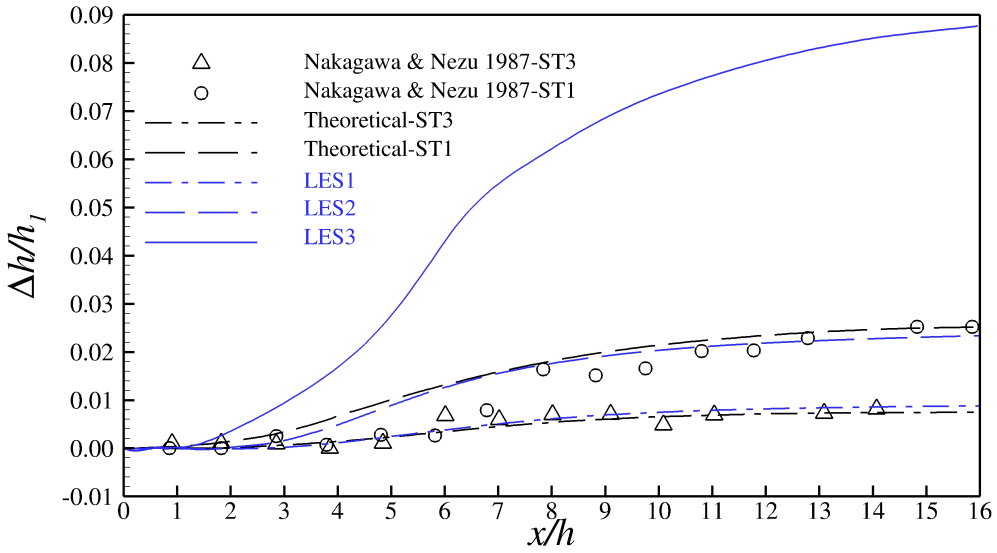

Figure 9 Water surface elevation as a function of streamwise distance from the step

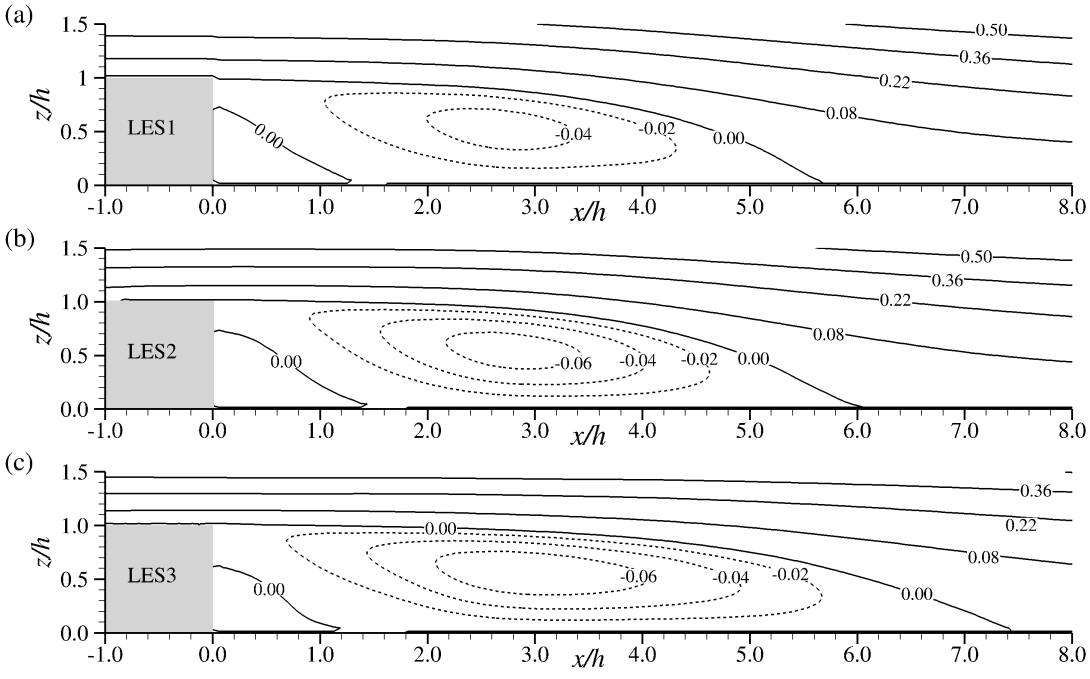

Figure 10 Time-averaged streamfunction of LES simulations

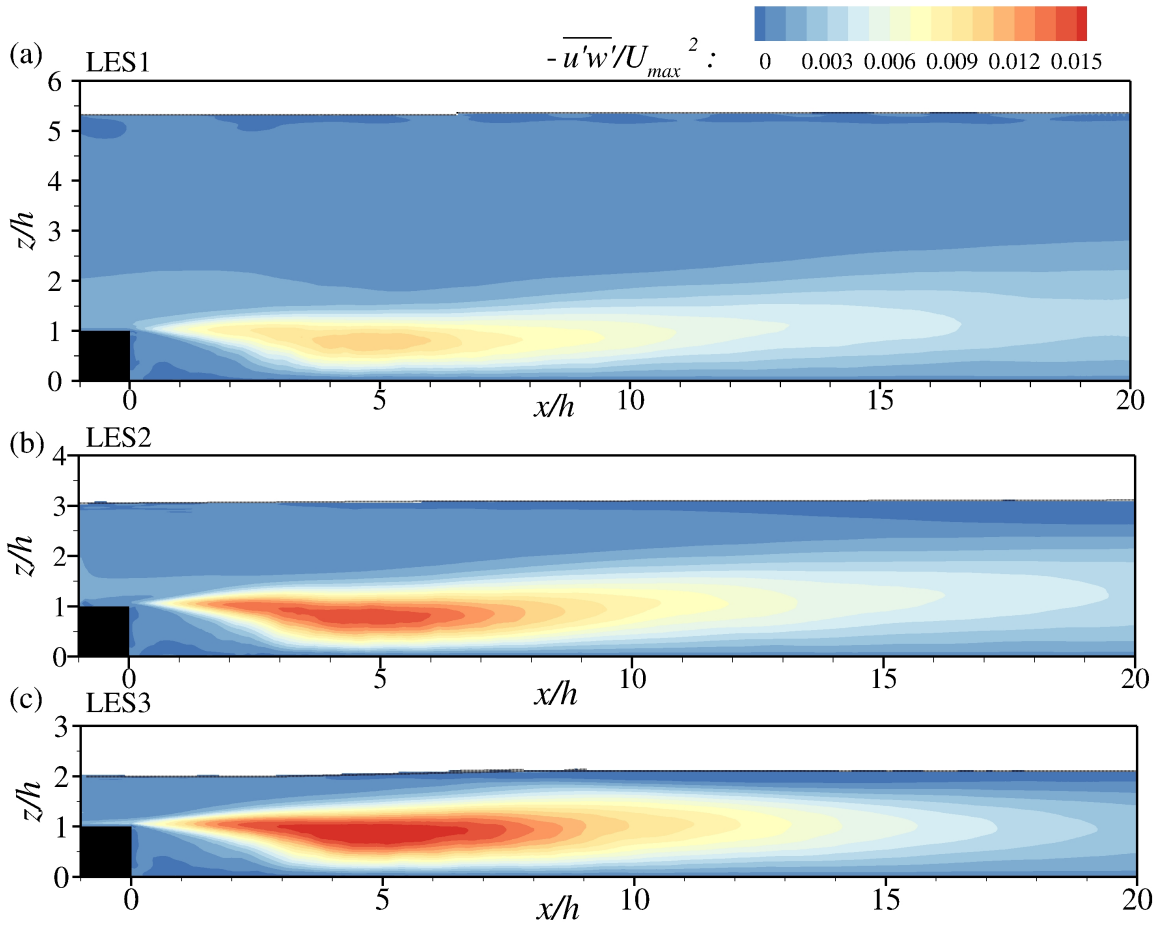

Figure 11 Contours of the normalised shear stress $-\overline{u'w'}/U_{max}^2$

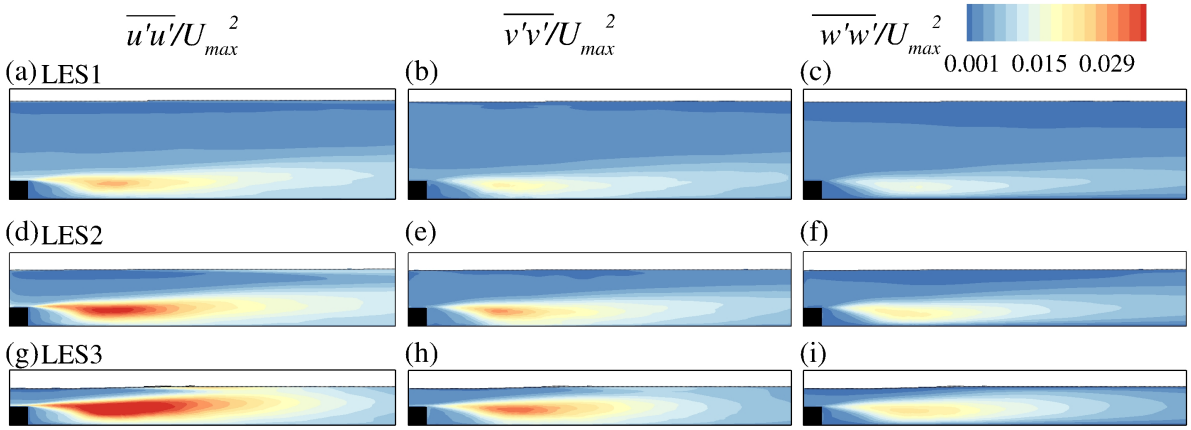

Figure 12 Contours of the normalised normal Reynolds stress $\overline{u'u'}/U_{max}^2$, $\overline{v'v'}/U_{max}^2$ and $\overline{w'w'}/U_{max}^2$

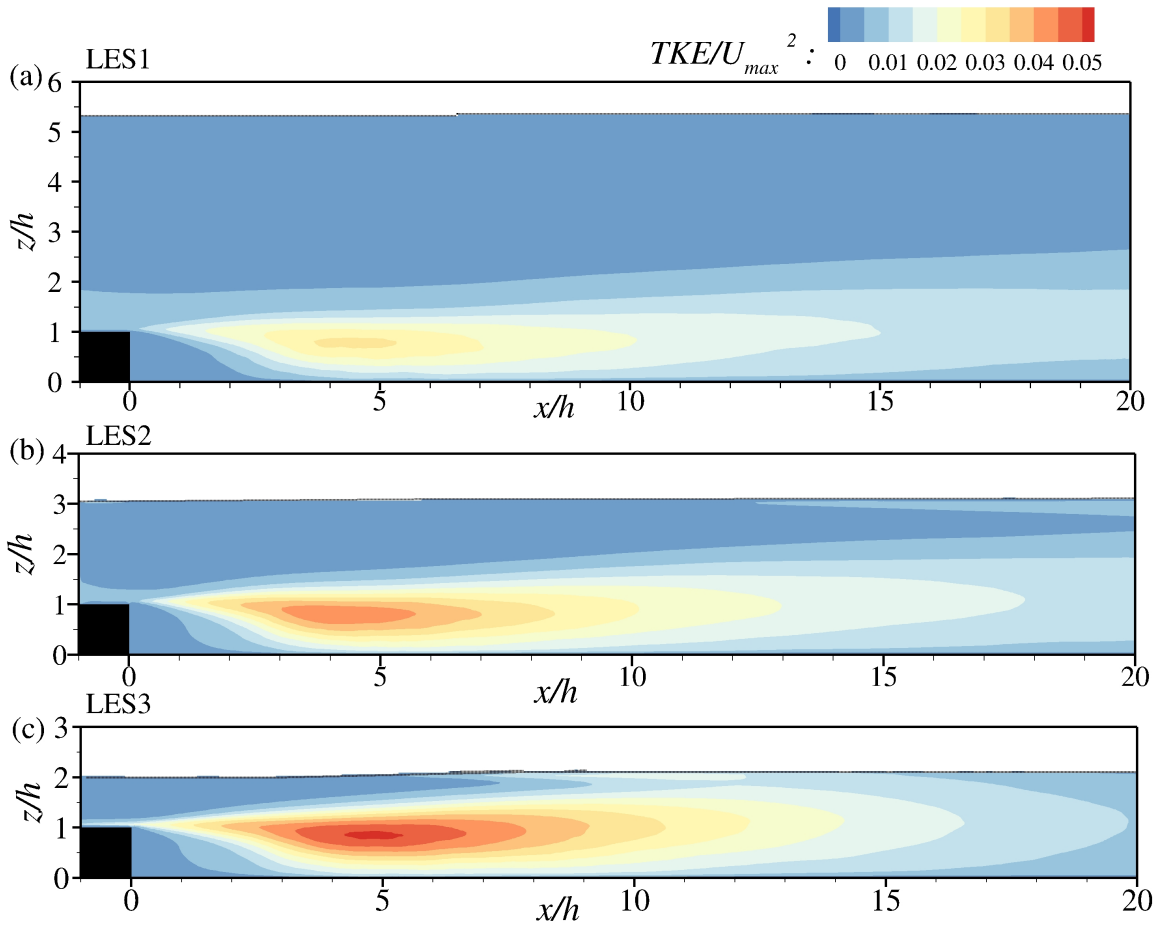

Figure 13 Contours of the normalised turbulent kinetic energy TKE/U_{max}^2

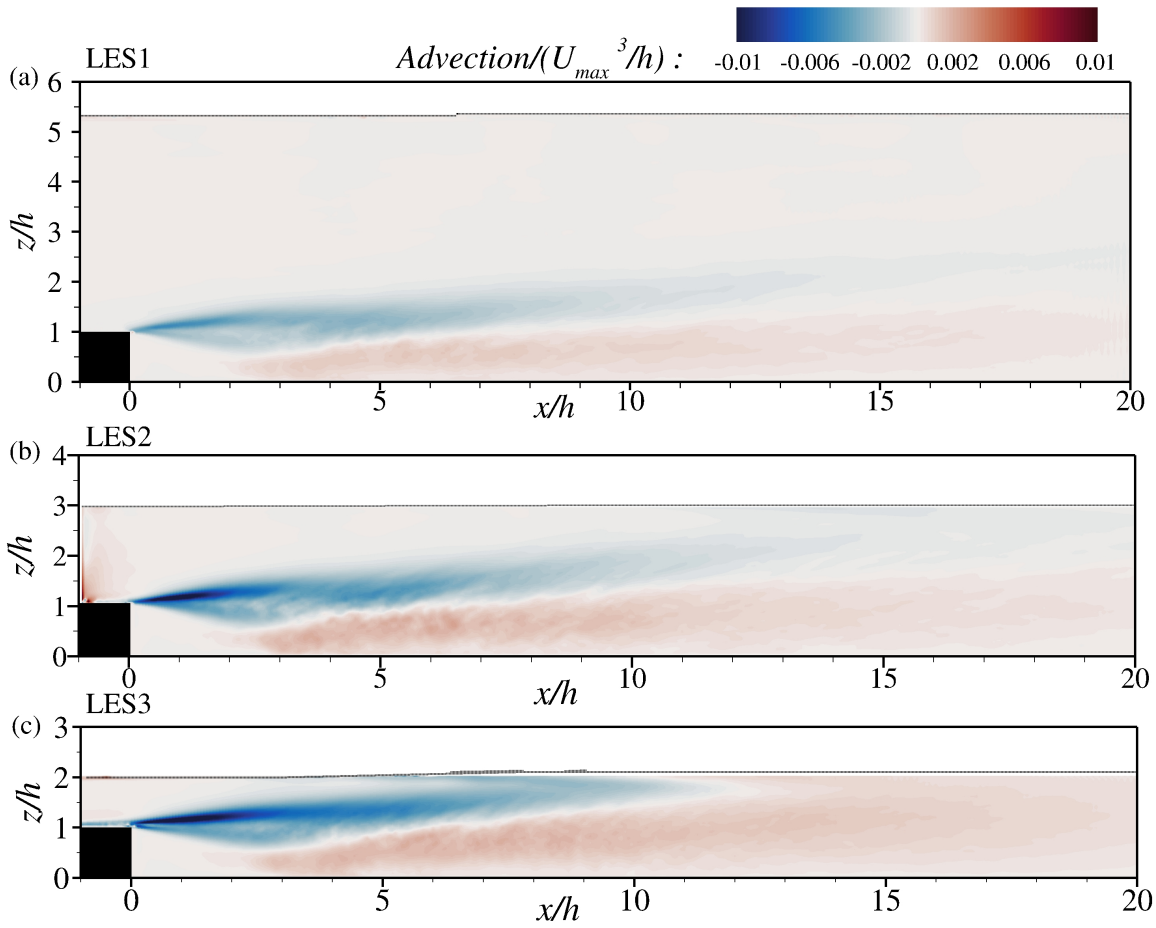

Figure 14 Distributions of advection in turbulent kinetic energy budget

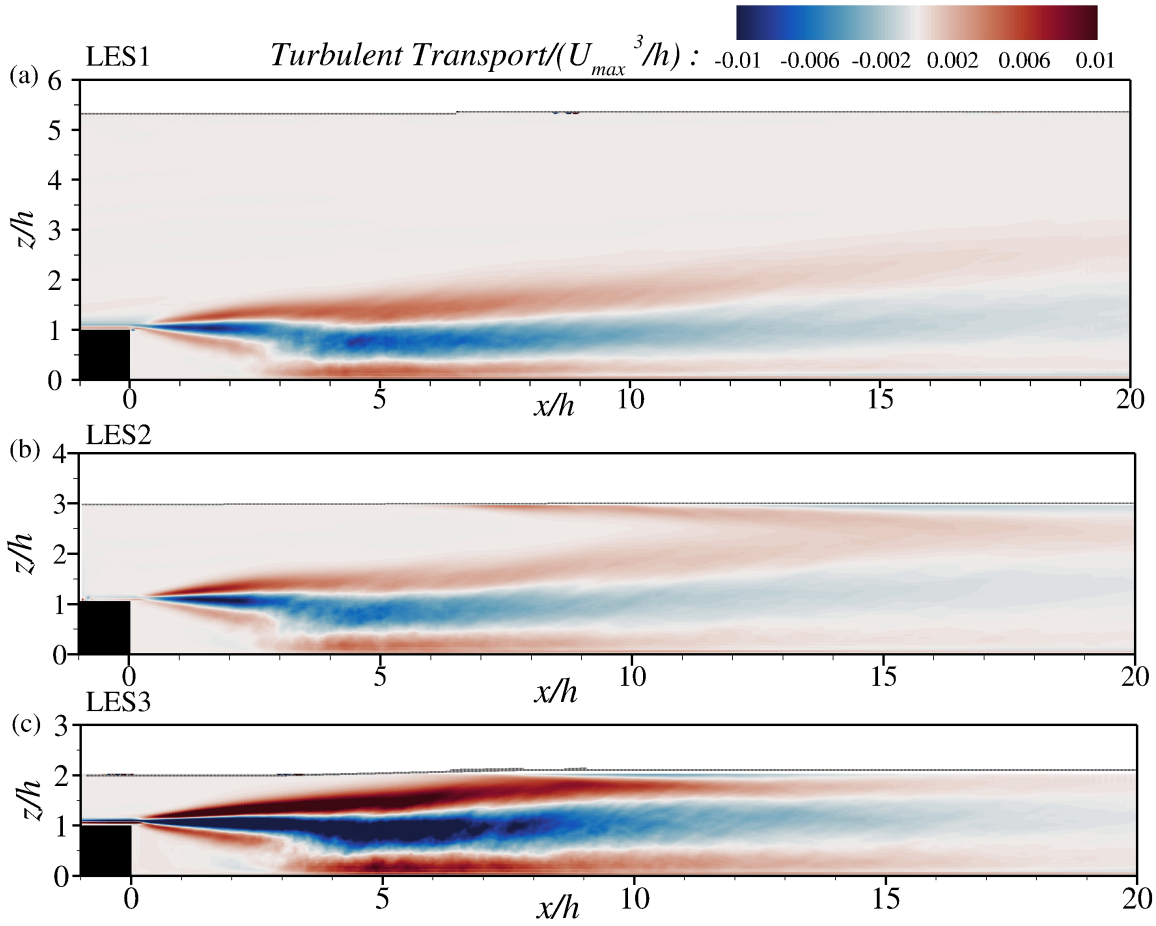

Figure 15 Distributions of turbulent transport in turbulent kinetic energy budget

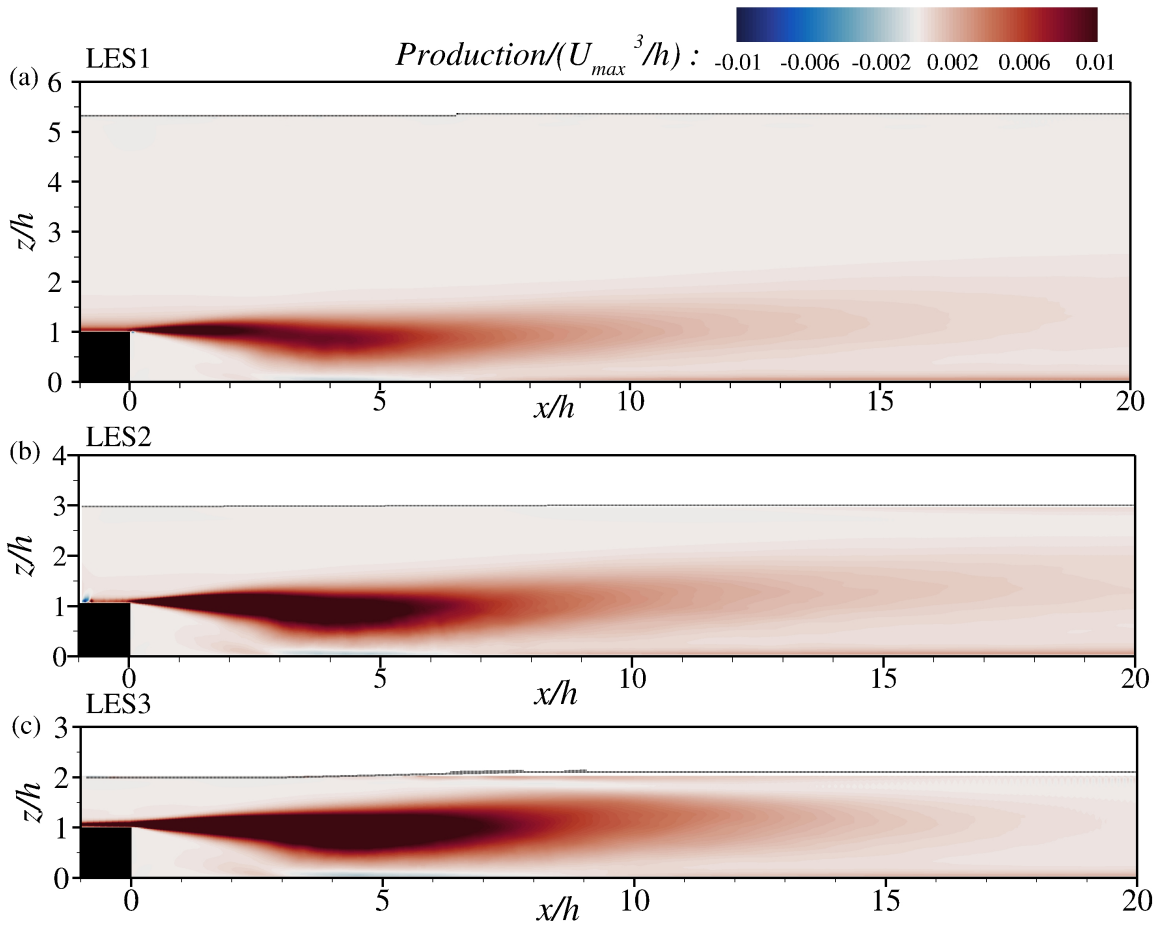

Figure 16 Distributions of production in turbulent kinetic energy budget

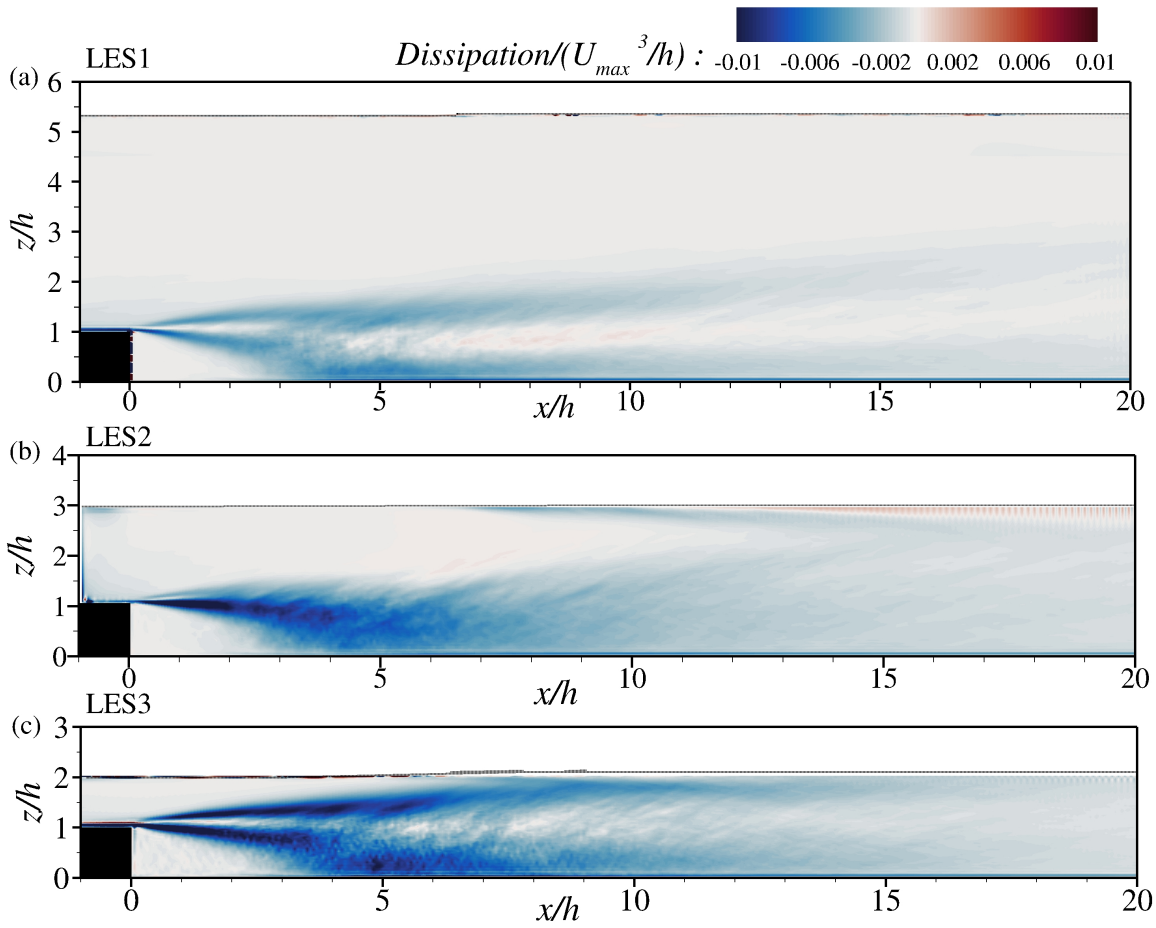

Figure 17 Distributions of dissipation in turbulent kinetic energy budget

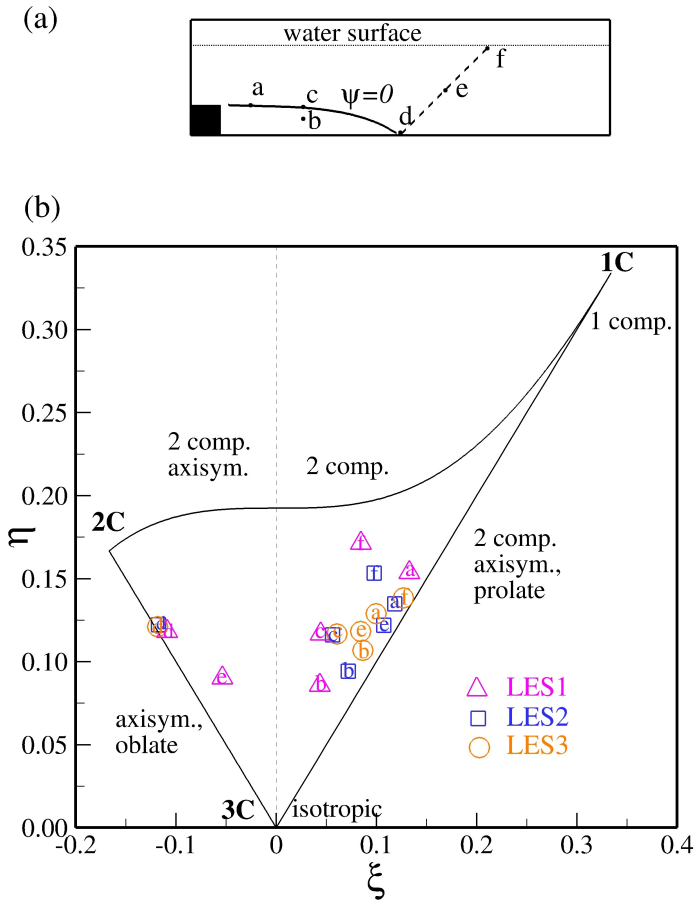

Figure 18 Lumley triangles analysis. (a) Sketch of selected locations; (b) Lumley triangle of different cases

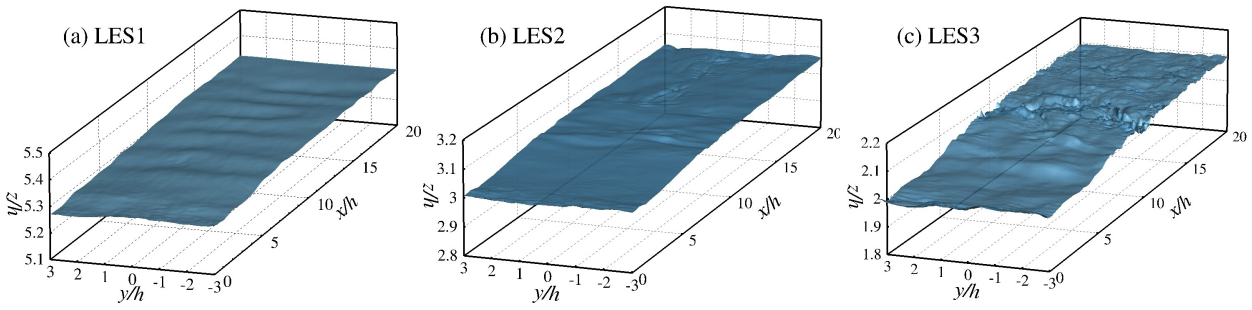

Figure 19 Instantaneous free surface (x:y:z=1:1:10)

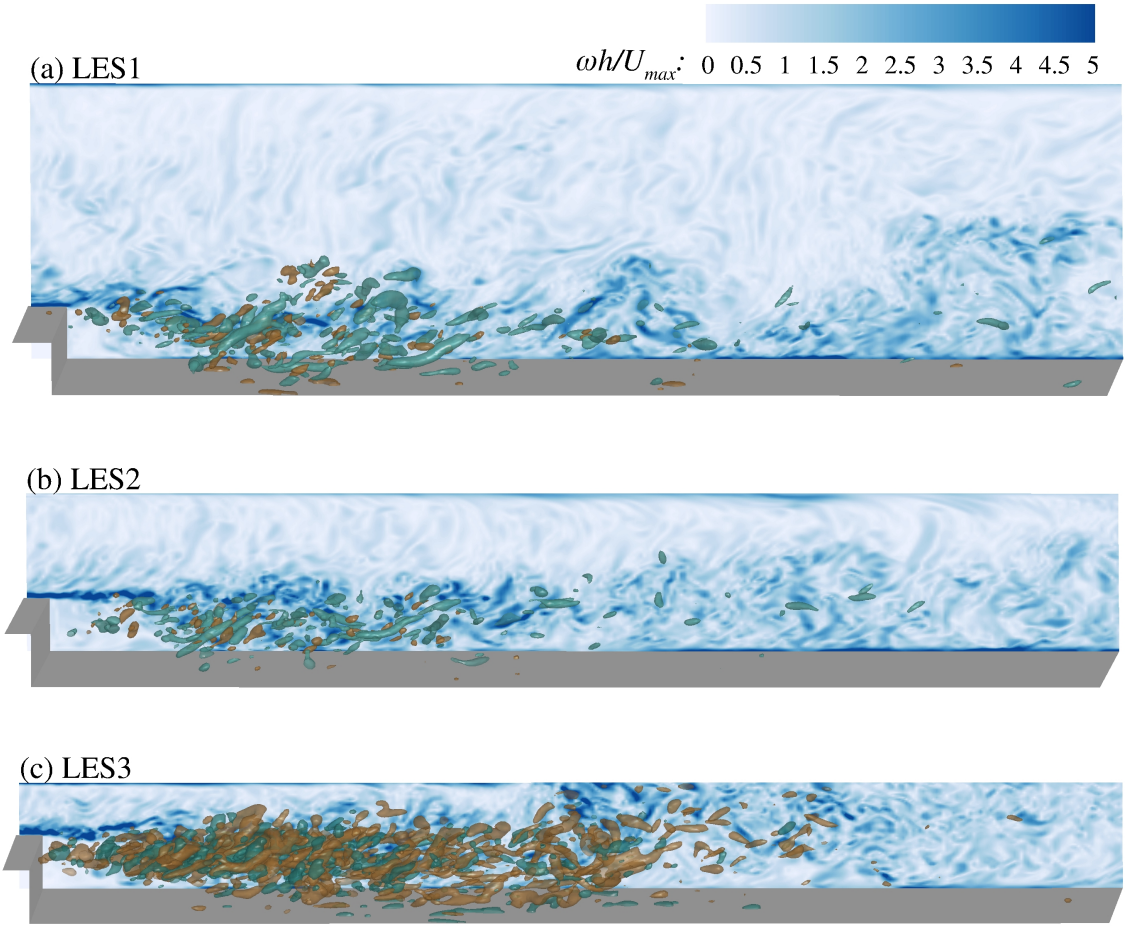

Figure 20 Isosurfaces of the Q-criterion (Q=-600 and Q=600) and contours of the normalised instantaneous vorticity magnitude in a longitudinal plane at an arbitrary instant in time

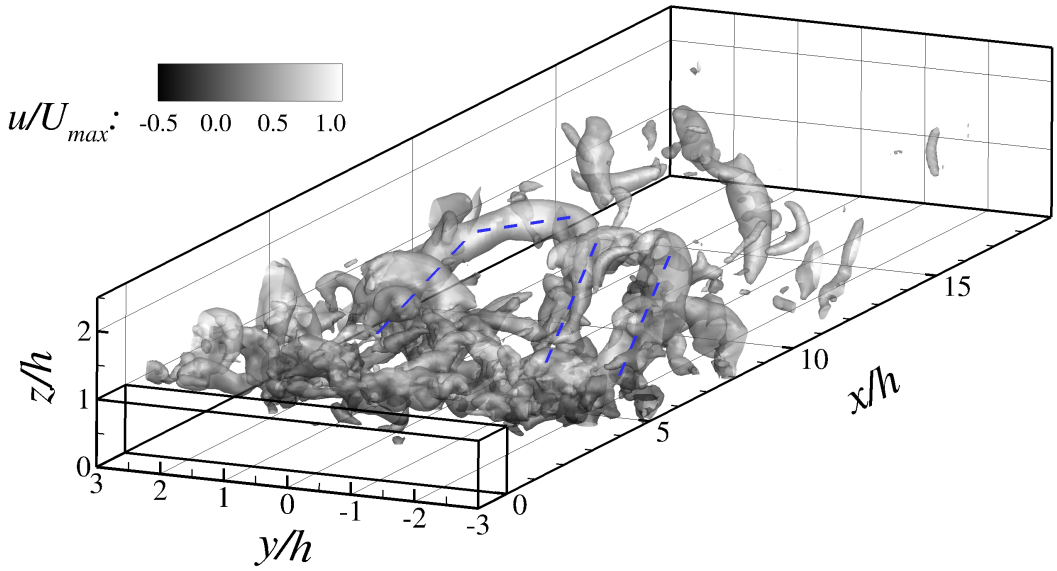

Figure 21 Isosurfaces of pressure fluctuations (contoured by normalised instantaneous streamwise velocity)

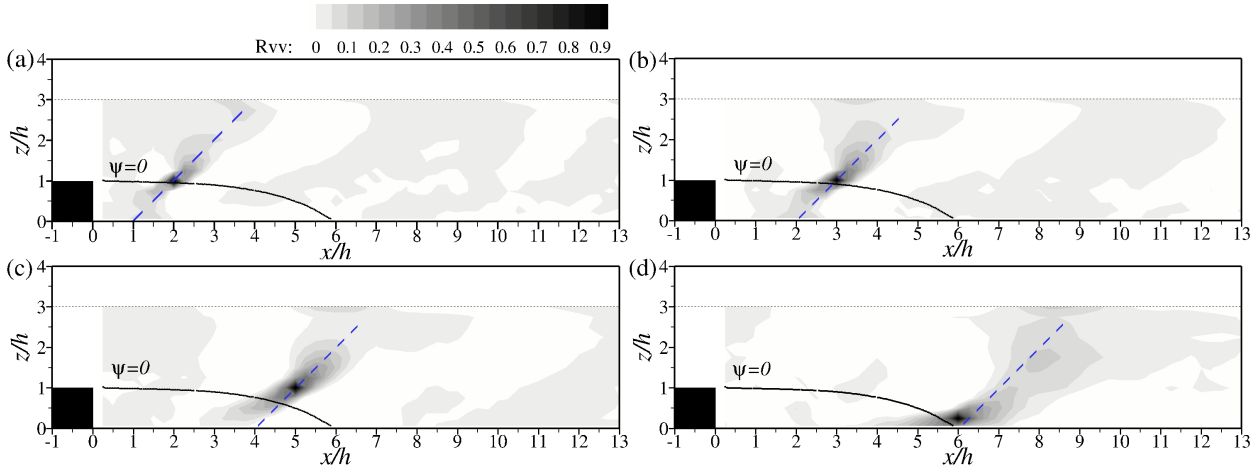

Figure 22 Distributions of auto-correlation function of LES2 with reference coordinates lies along the dividing streamline. Reference points are at (a) $x=2h,z=1h$, (b) $x=3h,z=1h$, (c) $x=5h,z=1h$ and (d) $x=6h,z=0.25h$

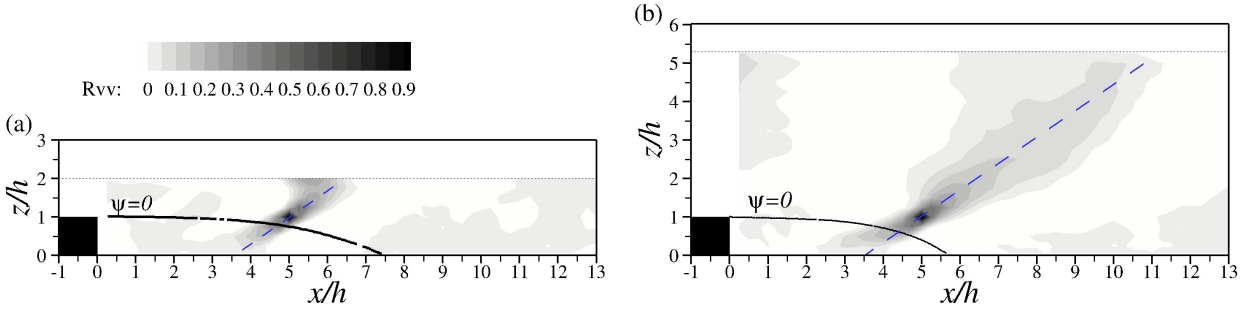

Figure 23 Distributions of auto-correlation function at reference coordinate at $x=5h, z=1h$. Left:LES3; Right:LES1

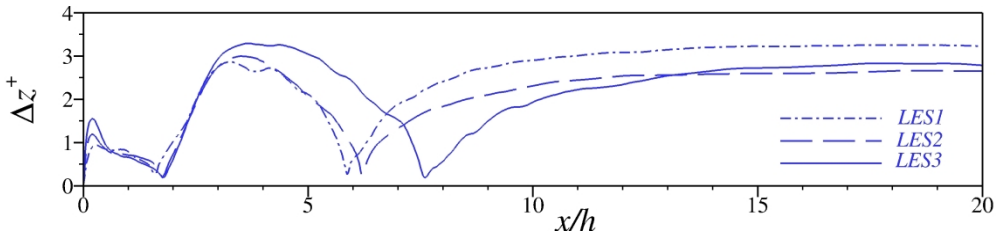

1058x238mm (72 x 72 DPI)

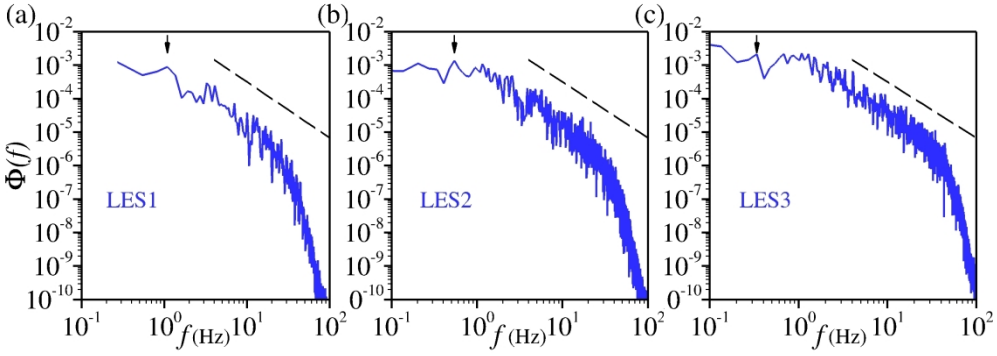

1058x375mm (72 x 72 DPI)

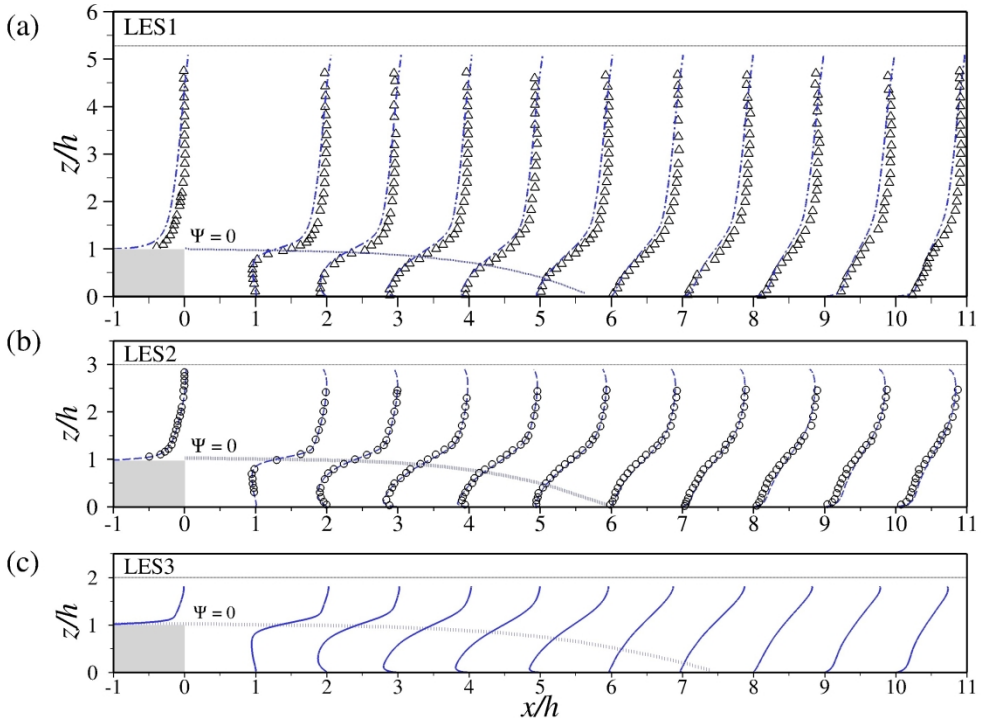

1013x724mm (72 x 72 DPI)

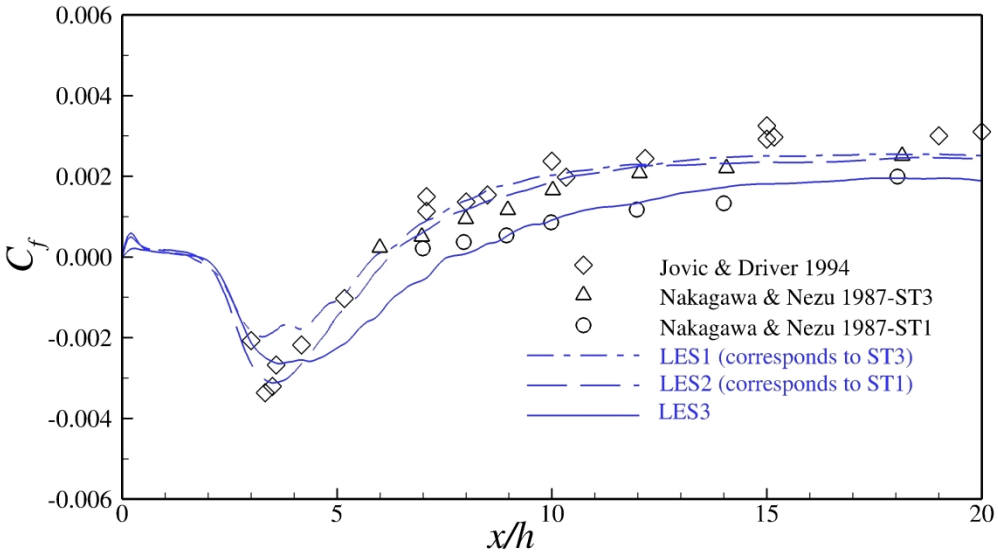

1058x588mm (72 x 72 DPI)

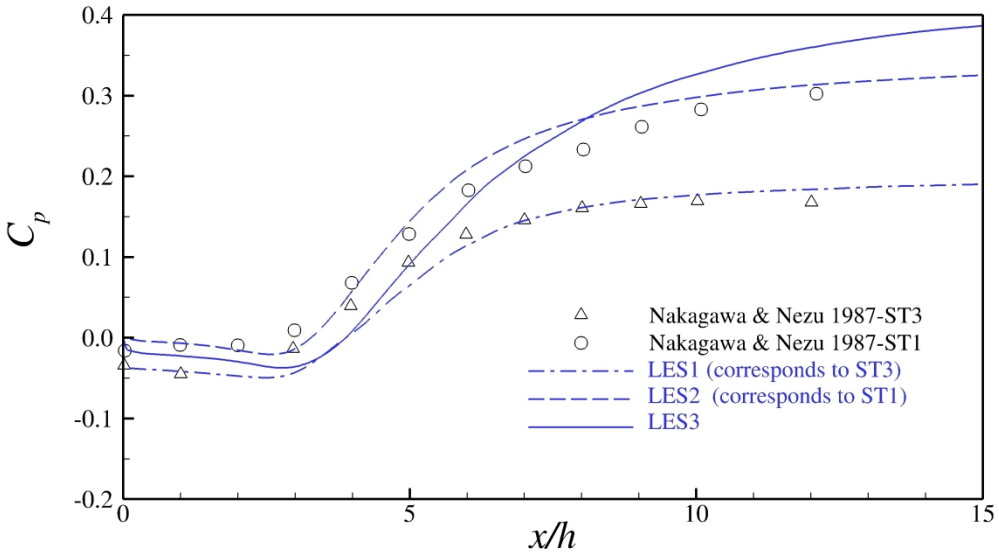

1058x588mm (72 x 72 DPI)

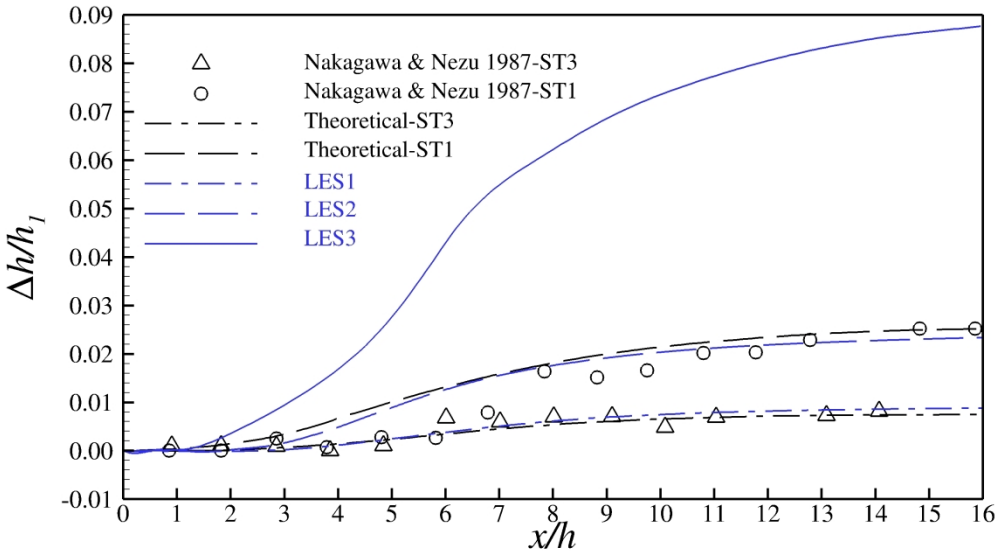

1058x588mm (72 x 72 DPI)

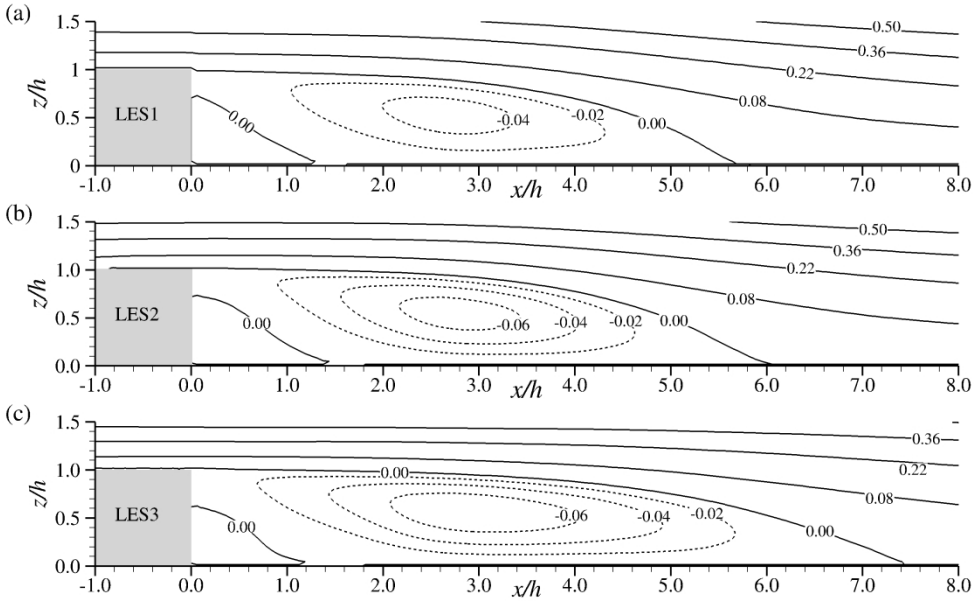

1058x635mm (72 x 72 DPI)

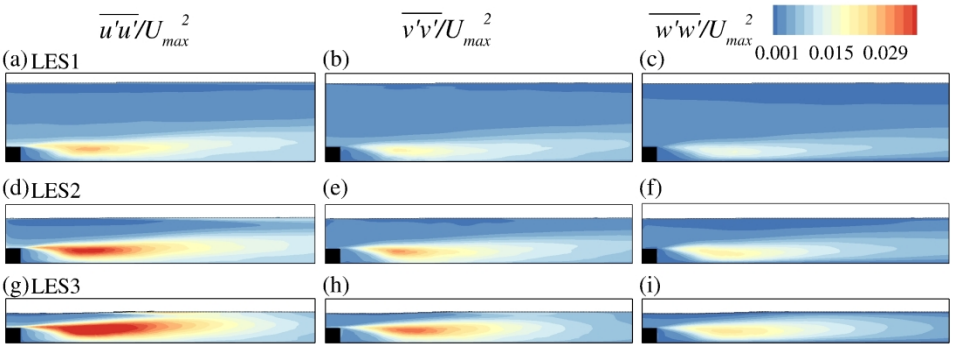

1058x412mm (72 x 72 DPI)

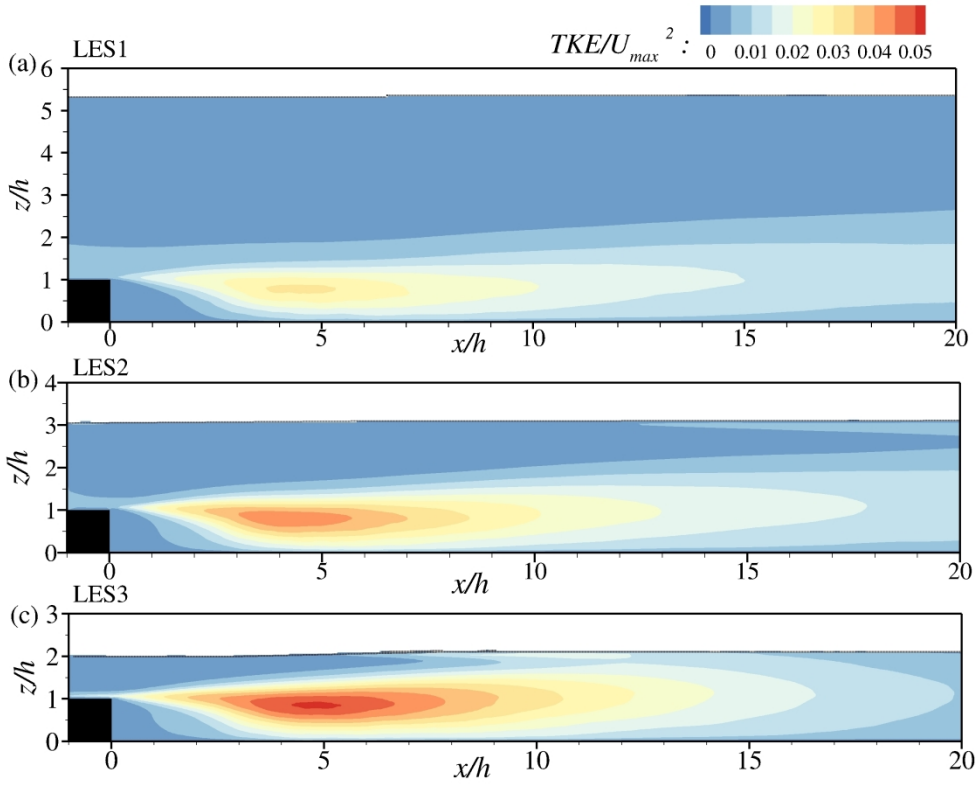

1058x839mm (72 x 72 DPI)

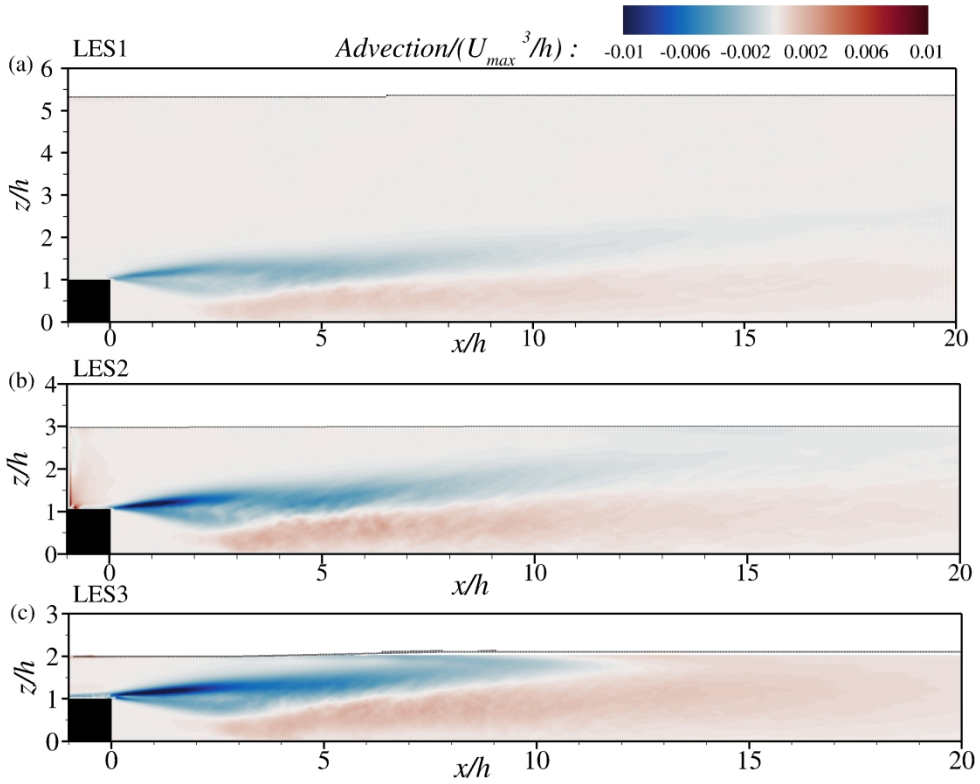

1058x839mm (72 x 72 DPI)

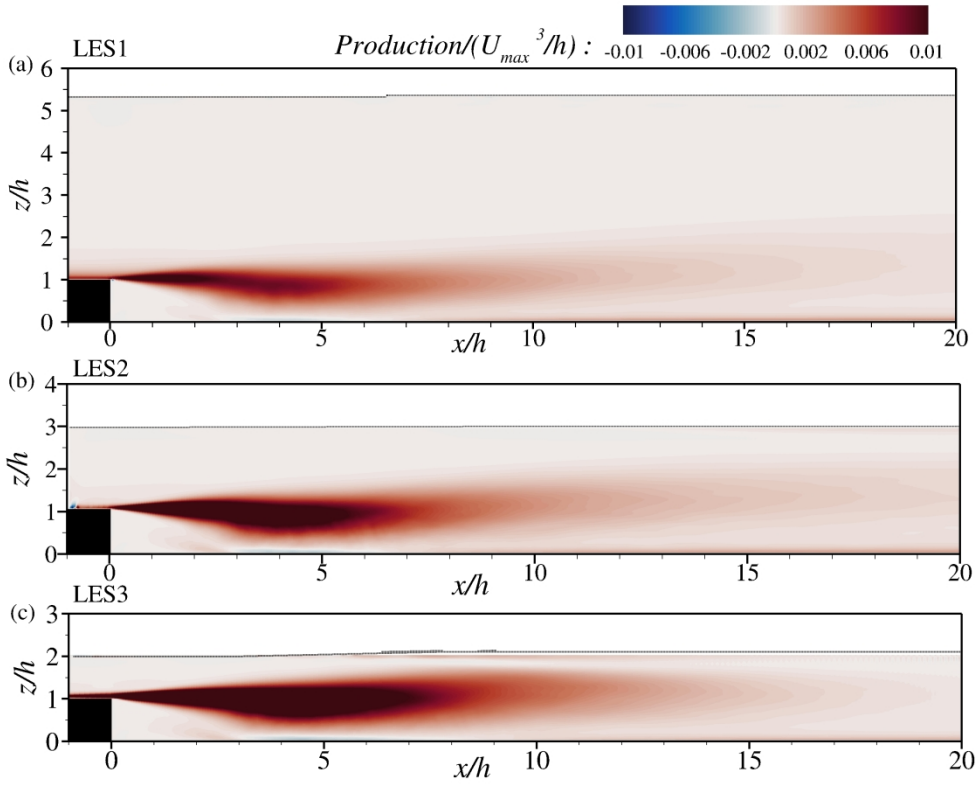

1058x839mm (72 x 72 DPI)

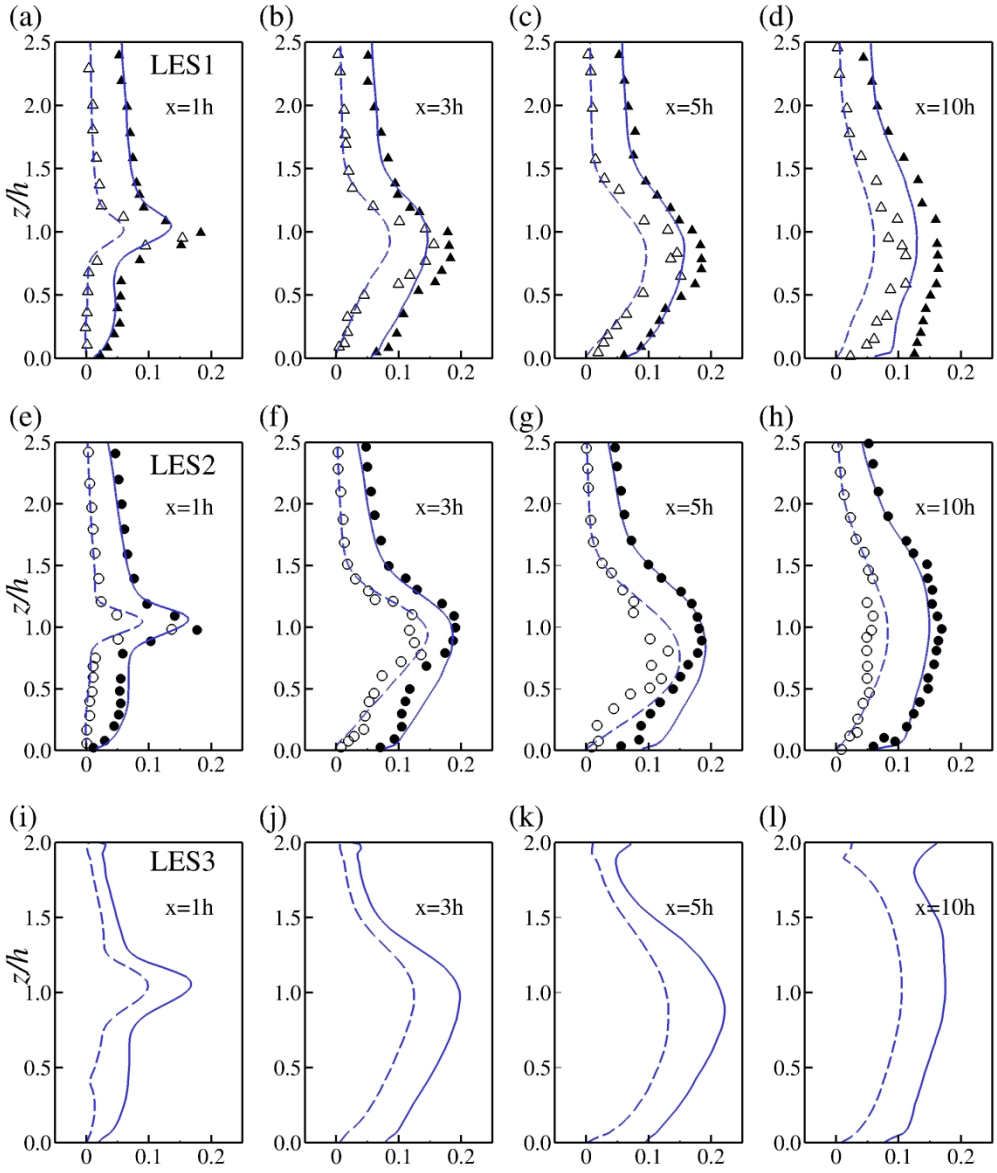

1058x1270mm (72 x 72 DPI)

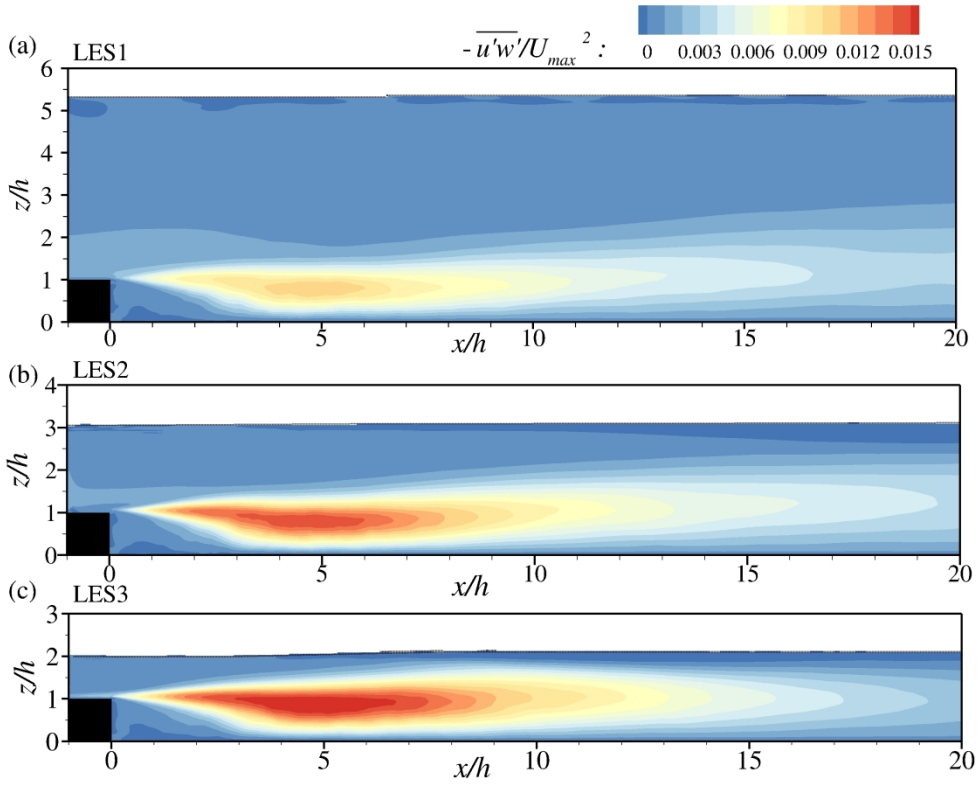

1058x839mm (72 x 72 DPI)

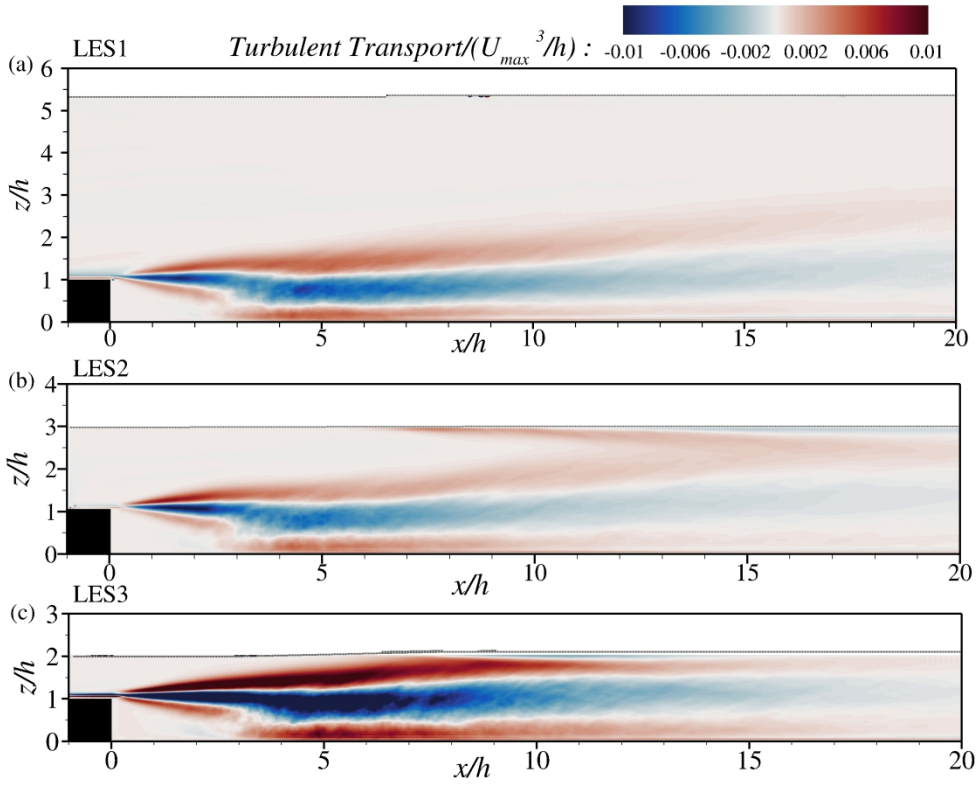

1058x839mm (72 x 72 DPI)

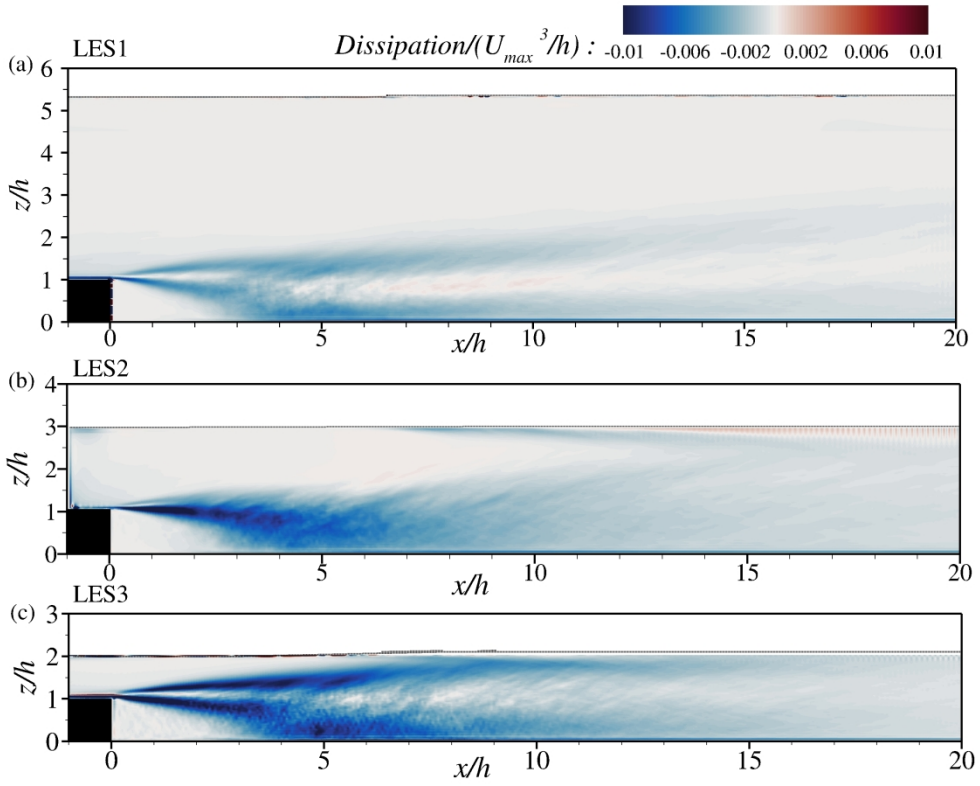

1058x839mm (72 x 72 DPI)

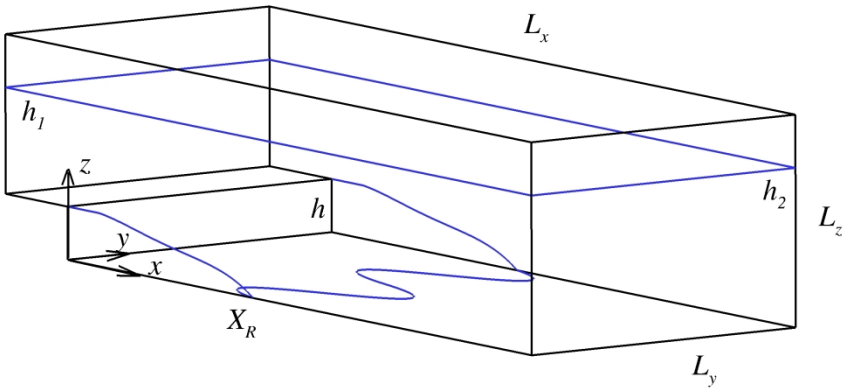

1058x510mm (72 x 72 DPI)

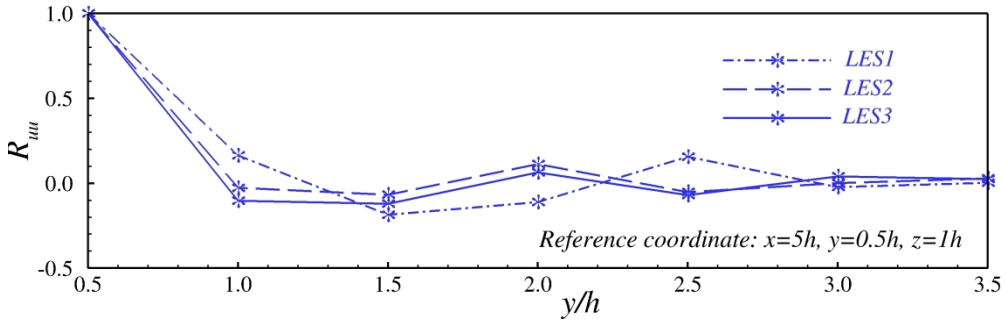

1058x339mm (72 x 72 DPI)

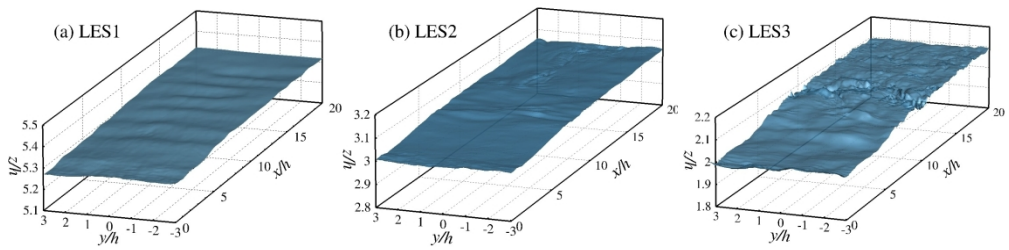

1053x257mm (72 x 72 DPI)

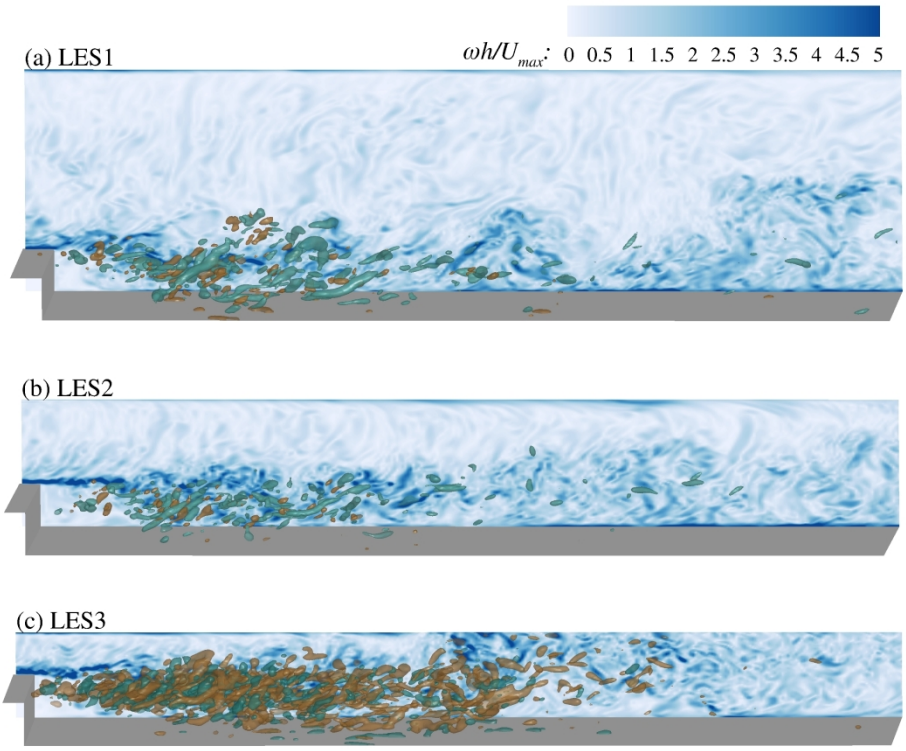

1058x810mm (72 x 72 DPI)

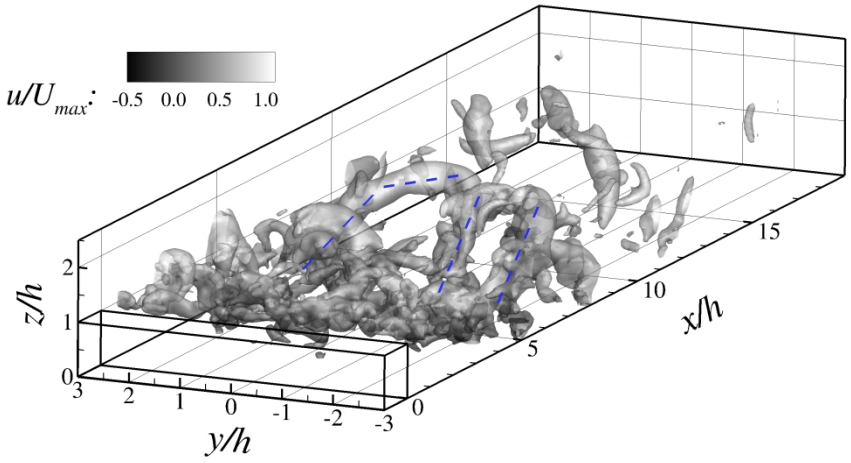

1058x529mm (72 x 72 DPI)

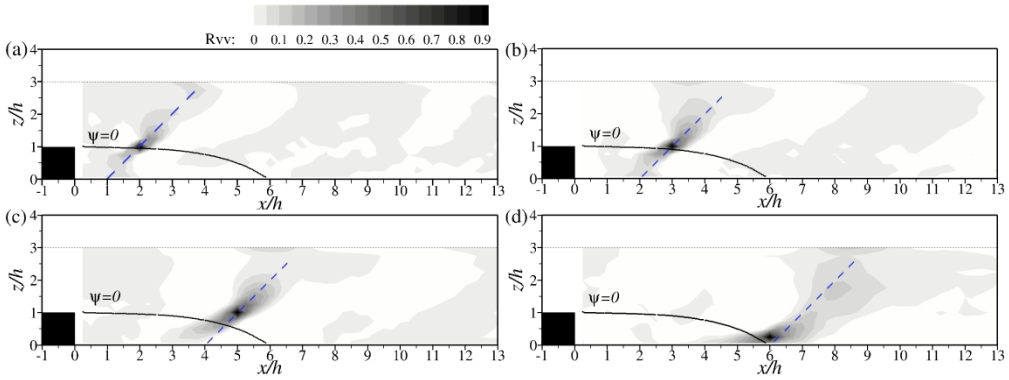

1058x397mm (72 x 72 DPI)

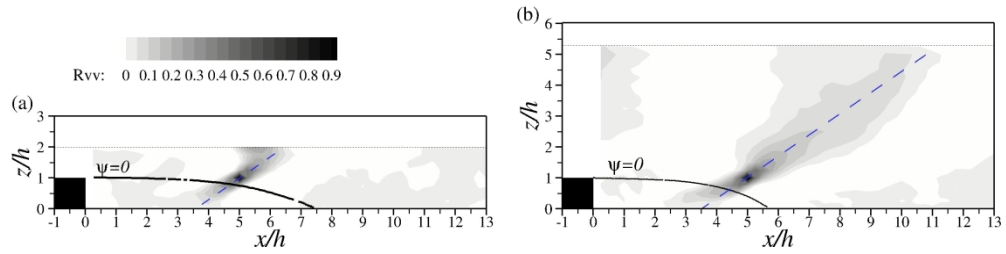

1041x254mm (72 x 72 DPI)

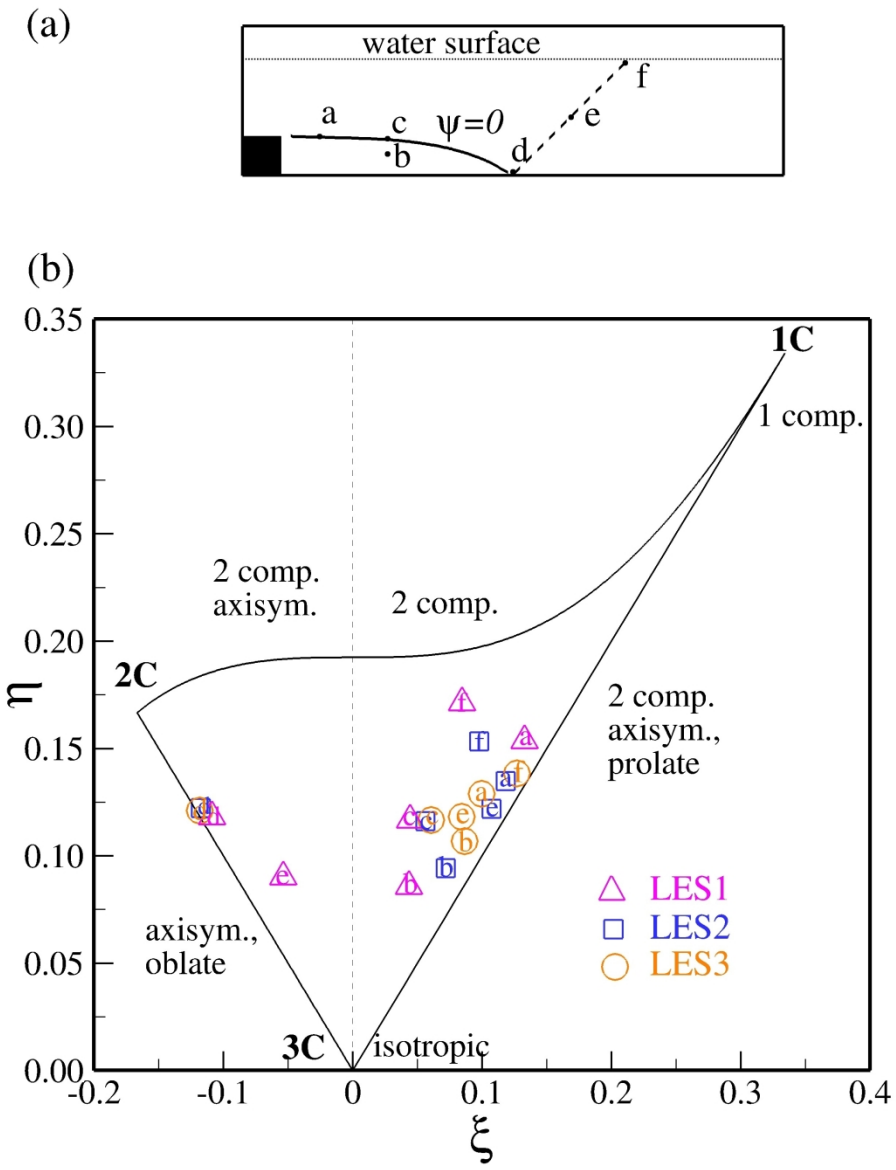

935x1162mm (72 x 72 DPI)